

# Modeling and simulation of the electrodynamic loudspeaker: a port-Hamiltonian approach

Antoine Falaize<sup>1,\*</sup>, Thomas Hélie<sup>1,\*</sup>

*Project-Team S3 (Sound Signals and Systems) and Analysis/Synthesis team, Laboratory of Sciences and Technologies of Music and Sound (UMR 9912), IRCAM-CNRS-UPMC,  
1 place Igor Stravinsky, F-75004 Paris*

---

## Abstract

The electrodynamic loudspeaker is a non-ideal transducer governed by mechanisms of mechanical, electromagnetic and thermal origins. A comprehensive modeling of these phenomena while guarantying elementary physical properties such as passivity and causality is not obvious. In this paper, we adopt the port-Hamiltonian systems formalism to decompose the system into conservative, dissipative and source parts, including for thermal modeling. This guarantees the passivity of continuous time models and the stability of the simulations for an adapted structure preserving numerical method. Three independent models are developed by elaborating on the standard Thiele/Small modeling. In particular, (i) a time-domain finite-dimensional state-space representation of the fractional dynamics associated with long term mechanical and magnetic memories and (ii) a simple albeit physically grounded formulation of the nonlinear dynamics of the magnetic flux in the pole piece are provided. Simulation results are exposed and prove in accordance with the literature.

*Keywords:* Electrodynamic loudspeaker, Multiphysics system, Port-Hamiltonian Systems, Passive Modeling, Numerical Method, Time Domain Simulation.

---

\*Corresponding author

Email address: [antoine.falaize@gmail.com](mailto:antoine.falaize@gmail.com) (Antoine Falaize)

<sup>1</sup>The contribution of both authors has been done at IRCAM, Paris, within the context of the French National Research Agency sponsored project HAMECMOPSY. Further information is available at <http://www.hamecmopsys.ens2m.fr>. The PhD thesis of A. Falaize is funded by the EDITE school from Paris.

## 1. Introduction

Electrodynamic loudspeakers are nonlinear transducers, which dynamics is governed by intricate multiphysical phenomena that are responsible for audio distortions [1, 2, 3]. First, the viscoelastic properties of the suspension material results in long term shape memory (linear) and hardening spring effect (non-linear). Second, the voice-coil includes a solid iron core charged by a strong magnet that is responsible for ferromagnetic saturation (nonlinear), and long time memory associated with eddy current losses (linear). Third, due to the DC resistance of coil wire, most of the provided electrical power is converted to heat which firstly changes the overall properties of the materials, and secondly is the principal cause of damages. A comprehensive modeling of these phenomena is the first step toward the development of DSP simulation-based real-time distortion compensation [4, 5, 6, 7] and burn-out protection methods [2, 8].

The electrodynamic loudspeaker dynamics is classically described by the linear time-invariant Thiele/Small modeling [9, 10, 11, 12], which is valid when the system is used in its linear operating region and during short periods. Refinements of the Thiele/Small structure have been proposed both in the frequency domain and the time domain [13, 14, 15, 16, 17, 18, 3]. The standard lumped-parameter approach [19, 1, 2, 20] consists in making the Thiele/Small parameters-dependent on some selected physical quantities (*e.g.* position-dependent stiffness). All these approaches can lead to models which physical interpretation is not obvious and, most importantly, the preservation of basic physical principles such as causality and passivity is not guaranteed. This is a critical point when considering long-time compensation or heat-protection application, since the stability of the numerical solution is not ensured. Other approaches are available, such as *gray-box* modeling techniques (Volterra and Wiener-Volterra series [21, 22, 23, 24], nonlinear ARMAX [25]) and finite element method [26, 27], but their use in a distortion compensation system of burn-out protection is not straightforward.

In this paper, we propose a comprehensive modeling of refined mechanical, electromagnetic, an thermal phenomena involved in the loudspeaker functioning, while preserving the inherent passivity of the original physical system. To that end, we adopt the *port-Hamiltonian systems* formalism, which provides a modular state-space representation of dynamical systems, structured according to power exchanges. This guarantee the passivity of the model in continuous time and the stability of the simulations in discrete-time. A simple low frequency approximation for the acoustical load is considered.

This paper is structured as follows. In section 2, the problem statement recalls the Thiele/Small model, discusses the multiphysical phenomena addressed in the sequel, and sets the scientific objectives. In section 3, the port-Hamiltonian framework is recalled along with examples. A slightly refined version of the Thiele/Small modeling (*model 0*) is presented that serves as the basis for the

elaboration of three loudspeaker models. Section 4 is concerned with the development of *model 1* which includes refined mechanical phenomena. In particular, a time domain finite dimensional state space representation of the fractional dynamics associated with viscoelastic long term memory is provided. Section 5 is  
 50 concerned with the development of *model 2* which includes refined electromagnetic phenomena. In particular, a simple albeit physically grounded formulation of the nonlinear dynamics of the magnetic flux in the pole piece is provided. Section 6 is concerned with the development of *model 3* which includes thermal phenomena. In particular, an extension of the standard port-Hamiltonian structure that cope with irreversible thermodynamics is presented. Models 1, 2  
 55 and 3 are independent. Simulation results are presented throughout the paper.

## 2. Problem statement

Firstly, this section presents an overview of the functioning of the electrodynamic loudspeaker and recalls the standard Thiele/Small modeling. Secondly,  
 60 it provides a survey of the main elementary multiphysical phenomena that are not tackled by this linear time invariant model. Thirdly, it establishes a list of the objectives and the scientific issues addressed in this paper.

### 2.1. Basic description and modeling

The basic functioning of a boxed loudspeaker such as the one depicted in figure 1 is as follows. A voice-coil ( $C$ ) is immersed in a magnetic field imposed by a permanent magnet ( $M$ ) in the air gap ( $G$ ) of a magnetic path (pole piece  $P$ ). The coil ( $C$ ) is glued to a large diaphragm ( $D$ ) which is maintained by a flexible suspension ( $S$ ). An input tension imposed to the coil ( $C$ ) induces a flow of electric charges through the wire (a current due to the self inductance of the coil). Each  
 65 moving charge in the magnetized air gap is imposed a force, orthogonal to the charge velocity and the magnetic induction field (Lorentz force). The resultant force experienced by the diaphragm is the sum of (i) the Lorentz force, (ii) the force due to the suspension ( $S$ ) (which includes spring effect and friction losses) and (iii) the acoustical load ( $A$ ).

70 The standard description of the dynamics of this system is referred as the Thiele/Small modeling, introduced in the early seventies [9, 10, 11, 12]. The electrical part ( $C$ ) includes the electrical resistance of the coil wire  $R_C$  and the linear approximation of the coil behavior with inductance  $L_C$ . The mechanical part ( $C,D,S,A$ ) is modeled as a damped harmonic oscillator with mass  $M_{CDA}$  (coil, diaphragm and additional mass due to acoustic radiation), linear approximation  
 75 of the spring effect  $K_{SA}$  (suspension and additional stiffness due to air compression in the enclosure) and fluid-like damping with coefficient  $R_{SA}$  (frictions and acoustic power radiation). The magnetic part ( $M,P,G,C$ ) reduces to a constant force factor  $B_\ell$ .

85

The corresponding set of ordinary differential equations are derived by applying Kirchhoff's laws to the electrical part ( $C$ ) and Newton's second law to

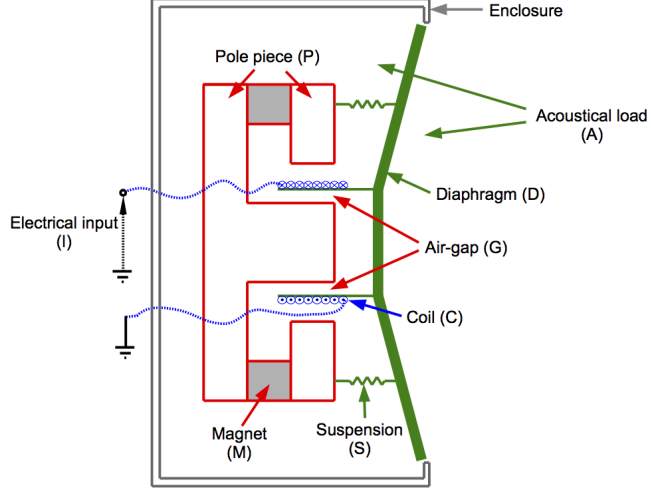


Figure 1: Schematic of the electrodynamic loudspeaker and components labels.

the mechanical part (D,S,A):

$$v_I(t) = v_L(t) + R_C i_C(t) + L_C \frac{di_C(t)}{dt}, \quad (1)$$

$$M_{CDA} \frac{d^2 q_D(t)}{dt^2} = f_L(t) - R_{SA} \frac{dq_D(t)}{dt} - K_{SA} q_D(t), \quad (2)$$

with  $v_I$  the input voltage,  $i_C$  the coil current and  $q_D$  the diaphragm's displacement (distance from equilibrium). The electro-mechanical coupling terms are the back electromotive force (tension)  $v_L = B_\ell \frac{dq_D}{dt}$  and the Lorentz force  $f_L = B_\ell i_C$ .

## 2.2. Refined multiphysics phenomena

The Thiele/Small model benefits from a good agreement with measurements for low excitation level, low to medium frequencies and short time measurements, but fails to capture several nonlinear and non-standard behaviors as detailed in e.g. [1, 2, 3] and references therein. The elementary phenomena responsible for significant audio distortions that are considered in this paper are thereafter listed.

### 2.2.1. Coupling phenomena

The electromechanical coupling (back e.m.f. and Lorentz force) depends on the coil (C) position with respect to the pole piece (P).

**Phenomenon 1** (Position-dependent force factor). *The fraction of coil wire subjected to the magnetic flux in the air gap depends on the coil position. This leads to consider a position-dependent effective wire length  $\ell(q_D)$  in the force factor  $B_\ell$  (see e.g. [1, figure 5]).*

Additionally, the coil acts as an electromagnet that changes the magnetic flux in the pole piece.

**Phenomenon 2** (Flux-dependent force factor). *The magnetic flux  $\phi_{PG}$  common to the air gap (G) and pole piece (P) depends on the magnetic flux induced in the coil due to an applied voltage (Faraday's law of induction). This leads to consider a flux-dependent magnetic induction  $B(\phi_{PG})$  in the force factor  $B_\ell$ .*

The electromagnetic coupling (coil inductive effect) also depends on the coil (C) position with respect to the pole piece (P).

**Phenomenon 3** (Position-dependent inductance). *The fraction of the coil core occupied by the pole piece depends on the coil position  $q_0$  (see e.g. [1, figure 6]). This leads to consider a position-dependent electromagnetic coupling between the electrical domain (C) and the magnetic domain (P).*

### 2.2.2. Mechanical phenomena

**120 Phenomenon 4** (Viscoelasticity). *The materials used for the suspension (S) exhibit combination of the behaviors of elastic solids and viscous fluid [28, §1.2], inducing long time shape memory (creep effect, see e.g. [28, figure 1] and [29, figure 11]).*

**125 Phenomenon 5** (Hardening suspension). *The materials used for the suspension (S) exhibit nonlinear stress-strain characteristics so that the restoring force is not proportional to the elongation [1, 18], with maximal instantaneous excursion  $q_{sat}$  that corresponds to the breakdown of the material.*

### 2.2.3. Electromagnetic phenomena

**135 Phenomenon 6** (Ferromagnetic saturation). *The materials used for the pole piece P exhibit nonlinear magnetic excitation-induction curve so that the equivalent current in the coil is not proportional to its magnetic flux. A maximal magnetic flux  $\phi_{sat}$  is reached (flux saturation), corresponding to the global alignment of the microscopic magnetic moments (see [30, §1], [31]).*

**140 Phenomenon 7** (Eddy currents losses). *Most of magnetic material (iron, cobalt, etc.) possess high electric conductivity. The application of a variable magnetic induction induces currents, namely eddy-currents, in a plane orthogonal to the field lines (see [32, §1.1.2]). This has three effects: (i) a power is*

*dissipated due to the natural resistivity of the material (Joule effect), (ii) eddy currents induces their own magnetic field (added inductive effect), and (iii) they oppose to the original induction (Lens's law), which pushes the field lines toward the boundary (magnetic skin effect).*

150

#### 2.2.4. Thermal phenomena

The coil wire exhibits a natural electrical resistivity (DC value of the electrical impedance) that transforms electrical power into heat by Joule effect, which is responsible of two phenomena.

155

**Phenomenon 8** (Heating of coil wire). *The coil wire temperature increases during the operating of the loudspeaker. This is the primary cause for damages of the device (see e.g. [13, 15]): either the resin on the voice coil melts causing short circuits, or the flux of the magnet structure is damaged causing loss of sensitivity and control.*

160

**Phenomenon 9** (Thermal compression). *The resistivity of the coil increases as the wire heats up, which increases the DC resistance and thus lowers the loudspeaker electroacoustics transduction efficiency (see e.g. [33, 8]).*

### 2.3. Objectives

165

The main objective of this work is to elaborate on the Thiele/Small modeling to provide lumped parameter loudspeaker models that include phenomena 1–9, while preserving basic physical principles such as passivity and causality. The second objective is to provide guaranteed-stable simulations of these models. To this end, we adopt the port-Hamiltonian (pH) approach which provides a modular framework that guarantees the passivity of the models and the stability of the simulations for an adapted numerical method.

170

## 3. Port-Hamiltonian systems (model 0)

175

The port-Hamiltonian (pH) formalism introduced in the 90's is a modular framework for the passive-guaranteed modeling of open dynamical systems. The key issue is the separation of (i) algebraic and differential constitutive relations attached to elementary components (*e.g.* mass, spring, resistor, magnet) from (ii) the interconnection scheme (glue point for mechanical components, schematic for electronic and magnetic components).

180

Firstly, the port-Hamiltonian framework will be recalled. Secondly, we will give two illustrative examples. Thirdly, the Thiele/Small modeling will be refined to cope with the force factor modulation (phenomenon 1). The result is recast as a port-Hamiltonian system (model 0) and simulation results will be shown.

### 3.1. Recall

Port-Hamiltonian systems are state space representations structured according to energy flows with state  $\mathbf{x} \in \mathbb{R}^{n_x}$ , input  $\mathbf{u} \in \mathbb{R}^{n_y}$ , output  $\mathbf{y} \in \mathbb{R}^{n_y}$  and storage function  $H(\mathbf{x}) \in \mathbb{R}_+$  (see [34, 35, 36] for details). Here, we consider the same algebraic-differential formulation as in [37], which includes a dissipation variable  $\mathbf{w} \in \mathbb{R}^{n_w}$  and a dissipation law  $\mathbf{z}(\mathbf{w}) \in \mathbb{R}^{n_w}$ :

$$\begin{pmatrix} \frac{d\mathbf{x}}{dt} \\ \mathbf{w} \\ -\mathbf{y} \end{pmatrix} = \underbrace{\begin{pmatrix} \mathbf{J}_{\mathbf{x}} & -\mathbf{K} & \mathbf{G}_{\mathbf{x}} \\ \mathbf{K}^T & \mathbf{J}_{\mathbf{w}} & \mathbf{G}_{\mathbf{w}} \\ -\mathbf{G}_{\mathbf{x}}^T & -\mathbf{G}_{\mathbf{w}}^T & \mathbf{J}_{\mathbf{y}} \end{pmatrix}}_{\mathbf{J}} \begin{pmatrix} \nabla H(\mathbf{x}) \\ \mathbf{z}(\mathbf{w}) \\ \mathbf{u} \end{pmatrix}, \quad (3)$$

with the Hamiltonian gradient  $(\nabla H(\mathbf{x}))_i = \frac{\partial H}{\partial x_i}$ ,  $\mathbf{K} \in \mathbb{R}^{n_x \times n_w}$ ,  $\mathbf{G}_{\mathbf{x}} \in \mathbb{R}^{n_x \times n_y}$ ,  $\mathbf{G}_{\mathbf{w}} \in \mathbb{R}^{n_w \times n_y}$  and the requirements that (i) the storage function  $H(\mathbf{x})$  is semi-positive definite  $H(\mathbf{x}) \geq 0$  with  $H(0) = 0$  and positive definite Hessian matrix  $[\mathcal{H}_H(\mathbf{x})]_{i,j} = \frac{\partial^2 H}{\partial x_i \partial x_j}(\mathbf{x})$ , (ii) the dissipation law  $\mathbf{z}(\mathbf{w})$  is null at origin  $\mathbf{z}(0) = 0$  with positive definite Jacobian matrix  $[\mathcal{J}_{\mathbf{z}}(\mathbf{w})]_{i,j} = \frac{\partial z_i}{\partial w_j}(\mathbf{w})$ , so that the dissipated power is  $P_D(\mathbf{w}) = \mathbf{z}(\mathbf{w})^T \mathbf{w} \geq 0$ ,  $P_D(0) = 0$  and (iii)  $\mathbf{J}_{\mathbf{x}} \in \mathbb{R}^{n_x \times n_x}$ ,  $\mathbf{J}_{\mathbf{w}} \in \mathbb{R}^{n_w \times n_w}$  and  $\mathbf{J}_{\mathbf{y}} \in \mathbb{R}^{n_y \times n_y}$  are skew-symmetric matrices, so that  $\mathbf{J}^T = -\mathbf{J}$ .

System (3) proves passive for the incoming power  $P_S = \mathbf{u}^T \mathbf{y}$  according to the following power balance:

$$\begin{pmatrix} \nabla H(\mathbf{x}) \\ \mathbf{z}(\mathbf{w}) \\ \mathbf{u} \end{pmatrix}^T \begin{pmatrix} \frac{d\mathbf{x}}{dt} \\ \mathbf{w} \\ -\mathbf{y} \end{pmatrix} = \frac{dH}{dt}(\mathbf{x}) + P_D(\mathbf{w}) - P_S = 0. \quad (4)$$

This proves the asymptotic stability of (3) in the sens of Lyapunov [38, §4].

### 3.2. Examples

The port-Hamiltonian approach is illustrated on the two systems in figure 2.

#### 3.2.1. Conservative system

Consider the harmonic oscillator in figure 2a, with  $n_x = 2$  (mass  $M$  and stiffness  $K$ ) and  $n_w = 0$  (no dissipation). We firstly describe the dynamics of the autonomous part with  $n_y = 0$  as follows:

*Linear oscillator.* The elongation of the spring equals the position of the mass w.r.t equilibrium, which is denoted by  $q$ . The Hamiltonian of the system is the sum of the kinetic and potential energies:  $H(\mathbf{x}) = H_M(x_1) + H_K(x_2)$ , with state  $\mathbf{x} = (p, q)^T$ , mass momentum  $p = M \frac{dq}{dt}$ , kinetic energy  $H_M(x_1) = \frac{x_1^2}{2M}$  and potential energy  $H_K(x_2) = \frac{Kx_2^2}{2}$ . The fictitious force of the mass is  $f_M = M \frac{d^2 q}{dt^2} = \frac{dx_1}{dt}$ , and its velocity is  $v_M = \frac{dq}{dt} = \frac{dx_2}{dt} = \frac{\partial H(\mathbf{x})}{\partial x_2}$ . The spring force is  $f_K = \frac{\partial H(\mathbf{x})}{\partial x_2} = Kx_2$ ,

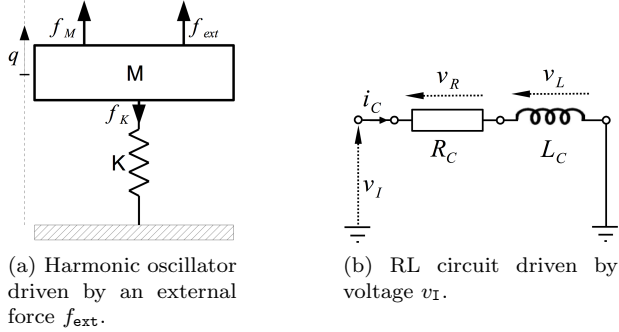


Figure 2: Examples addressed in section 3.2.

and the mass is glued to the spring so that  $v_K = v_M$ . This corresponds to a standard Hamiltonian dynamics [39]:

$$\underbrace{\begin{pmatrix} \frac{dp}{dt} \\ \frac{dq}{dt} \end{pmatrix}}_{\frac{dx}{dt}} = \underbrace{\begin{pmatrix} 0 & -1 \\ 1 & 0 \end{pmatrix}}_{J_x} \underbrace{\begin{pmatrix} \frac{p}{M} \\ \frac{q}{K} \end{pmatrix}}_{\nabla H(x)}. \quad (5)$$

*Nonlinear oscillator.* Consider the replacement of the (linear) stiffness  $K$  by a nonlinear spring  $S$  with constitutive law  $f_S(q) = \sum_{n=0}^N K_n q^{2n+1}$ , designed such that the associated potential energy  $H_S(q) = \int_0^q f_S(x) dx = \sum_{n=0}^N \frac{K_n}{2(n+1)} q^{2(n+1)}$  is positive definite for the  $K_n \geq 0$ . The dynamics is still given by (5) for the new Hamiltonian  $H(x) = H_M(x_1) + H_S(x_2)$ .

*External port.* Consider now the non-autonomous system in figure 2a with arrangement of variables as input  $\mathbf{u} = (f_{\text{ext}})^\top$  (applied force) and output  $\mathbf{y} = (v_{\text{ext}})^\top = (v_M)^\top$  (velocity) so that the external work performed on the system is  $W = f_{\text{ext}} q$  and the provided external power is  $P_S = \mathbf{u}^\top \mathbf{y}$ . The dynamics is

$$\begin{pmatrix} \frac{dp}{dt} \\ \frac{dq}{dt} \\ -v_{\text{ext}} \end{pmatrix} = \left( \begin{array}{cc|c} 0 & -1 & 1 \\ 1 & 0 & 0 \\ -1 & 0 & 0 \end{array} \right) \begin{pmatrix} \frac{p}{M} \\ \frac{q}{K} \\ f_{\text{ext}} \end{pmatrix} \quad (6)$$

which restores the form (3) for the structure in table 1.

*Simulation.* A dedicated numerical method that preserves the port-Hamiltonian structure (3) in discrete time is available for simulations (see [40] and AppendixA). This guarantees a numerical power balance (and hence, a numerical stability) as shown in figure 3.

### 3.2.2. Strictly passive system

Port-Hamiltonian systems (3) are not restricted to the “classical Hamiltonian systems” [39], for which  $n_w = 0$ ,  $n_x$  is even and  $J_x$  is similar to  $J_x^* = \begin{pmatrix} 0_{n_x/2} & -\mathbb{I}_{n_x/2} \\ \mathbb{I}_{n_x/2} & 0_{n_x/2} \end{pmatrix}$ ,

State: $\mathbf{x} = (p, q)^\top$	Energy: linear $H(\mathbf{x}) = \frac{x_1^2}{2M} + \frac{Kx_2^2}{2}$ nonlinear $H(\mathbf{x}) = \frac{x_1^2}{2M} + \frac{K_0x_2^2}{2} + \frac{K_1x_2^4}{4}$
Dissipation variable: $\mathbf{w} \equiv \text{none}$	Dissipation law: $\mathbf{z}(\mathbf{w}) \equiv \text{none}$
Input: $\mathbf{u} = (f_{\text{ext}})^\top$	Output: $\mathbf{y} = (v_{\text{ext}})^\top$
	Structure: $\mathbf{J}_x = \begin{pmatrix} 0 & -1 \\ 1 & 0 \end{pmatrix}, \mathbf{G}_x = \begin{pmatrix} 1 \\ 0 \end{pmatrix}, \mathbf{J}_y = 0,$ $\mathbf{K} \equiv \text{none}, \mathbf{J}_w \equiv \text{none}, \mathbf{G}_w \equiv \text{none}.$

Table 1: Port-Hamiltonian formulation (3) for the harmonic oscillator depicted in figure 2a with mass position  $q$  and momentum  $p = M \frac{dq}{dt}$ , external force  $f_{\text{ext}}$  and no dissipation component.

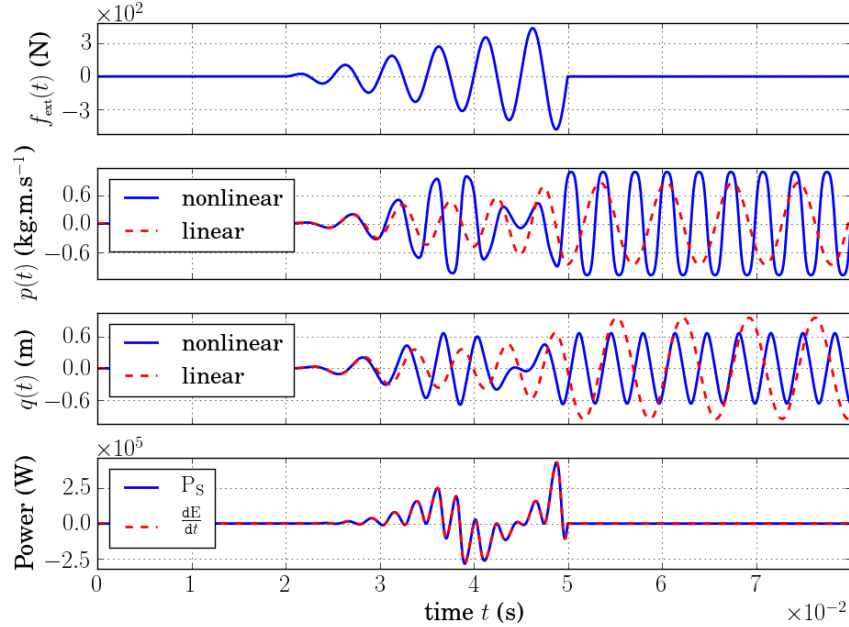


Figure 3: Dynamics for the conservative oscillator driven with the external force  $f_{\text{ext}}$  described in table 1. Parameters are  $M = 10^{-3}\text{Kg}$ ,  $K = K_0 = 800\text{N.m}^{-1}$  and  $K_1 = 8000\text{N.m}^{-3}$ . The external force is a 200Hz sine wave with increasing amplitude between 0 and 500N. The sampling rate is  $F_s = 20\text{kHz}$ . The power balance is shown for the nonlinear case only.

for symplectic coordinates. For pH systems,  $\mathbf{J}_x$  can even be rank deficient, as exemplified through the RL circuit depicted in figure 2b (simplest modeling of a coil (C) with self inductance  $L_C$  and wire resistance  $R_C$ ). This system is made

215 of  $n_x = 1$  storage element (inductance  $L_c$ ),  $n_w = 1$  dissipative element (resistance  $R_c$ ) and  $n_y = 1$  external port (input tension  $v_I$ ). The state associated with the inductor is the total magnetic flux  $\mathbf{x} = (\phi)^\top$  with  $\phi = \int_0^t v_L(\tau) d\tau$ , and the Hamiltonian corresponds to the electrodynamic energy  $H(\mathbf{x}) = \frac{x_1^2}{2L_c}$  so  
 220 that  $i_c = \frac{\partial H}{\partial x_1} = \frac{x_1}{L_c}$ . The dissipation variable is chosen as  $\mathbf{w} = (i_c)^\top$  with linear dissipation law  $\mathbf{z}(\mathbf{w}) = (R_c w_1)^\top$ . The port variables are arranged as input  $\mathbf{u} = (v_I)^\top$  and output  $\mathbf{y} = (i_c)^\top$ . Applying kirchhoff's laws, this system is recast as a port-Hamiltonian system (3) for the definition in table 2.

State: $\mathbf{x} = (\phi)^\top$	Energy: $H(\mathbf{x}) = \frac{x_1^2}{2L_c}$
Dissipation variable: $\mathbf{w} = (i_c)^\top$	Dissipation law: $\mathbf{z}(\mathbf{w}) = (R_c w_1)^\top$
Input: $\mathbf{u} = (v_I)^\top$	Output: $\mathbf{y} = (i_c)^\top$
Structure: $\mathbf{J}_x = 0, \mathbf{K} = 1, \mathbf{G}_x = 1,$ $\mathbf{J}_w = 0, \mathbf{G}_w = 0, \mathbf{J}_y = 0.$	

Table 2: Port-Hamiltonian formulation (3) for the RL circuit depicted in figure 2b with magnetic flux  $\phi$  and input tension  $v_I$ .

### 3.3. Port-Hamiltonian formulation of loudspeaker dynamics (model 0)

225 The Thiele/Small modeling from section 2.1 can be regarded as the interconnection of a RL circuit with a mass-spring-damper system, through a gyrator that describes the reversible energy transfer from the electrical domain to the mechanical domain as depicted in figure 4 and detailed in AppendixB.2.

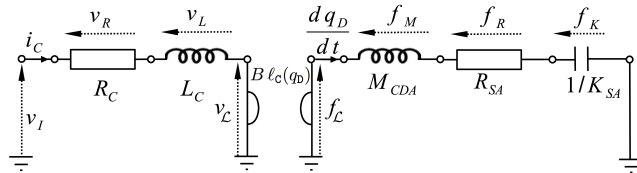


Figure 4: Equivalent circuit of the model 0 with direct electromechanical analogy (force=voltage, velocity=current). It corresponds to the Thiele/Small model (1)-(2) with position-dependent electromechanical coupling (phenomenon 1) that restores the gyrator (B.3) with the force factor  $B \ell_c(q_0)$  for the effective wire length  $\ell_c(q_0)$  in (8).

*Description.* This system includes  $n_x = 3$  storage components (coil inductance  $L_c$ , mass  $M_{CDA}$  and stiffness  $K_{SA}$ ),  $n_w = 2$  dissipative components (electrical

230 resistance  $R_c$  and mechanical damping  $R_{SA}$ ) and  $n_y = 1$  port (electrical input  $v_I$ ). The state  $\mathbf{x} = (\phi_c, p_M, q_D)^\top$  consists of the magnetic flux in the coil  $\phi_c$ , mass momentum  $p_M = M_{CDA} \frac{dq_D}{dt}$  and diaphragm position  $q_D$ . The Hamiltonian is the sum of the electrodynamic energy  $H_L(x_1) = \frac{x_1^2}{2\ell_c^2}$ , the kinetic energy  $H_M(x_2) = \frac{x_2^2}{2M_{CDA}}$  and the potential energy  $H_K(x_3) = K_{SA} \frac{x_3^2}{2}$ . The dissipation variable is  $\mathbf{w} = (i_c, \frac{dq_D}{dt})^\top$  with linear dissipation law  $\mathbf{z}(\mathbf{w}) = \text{diag}(R_c, R_{SA}) \mathbf{w}$ .

235 *Position-dependent force factor (model 0).* The gyrator that restores the Lorentz force  $f_L$  with corresponding back electromotive force  $v_L$  is given in (B.3) and recalled below:

$$\begin{pmatrix} v_L \\ f_L \end{pmatrix} = \begin{pmatrix} 0 & -B \ell_c \\ B \ell_c & 0 \end{pmatrix} \begin{pmatrix} i_c \\ v_c \end{pmatrix}, \quad (7)$$

with coil velocity  $v_c = \frac{dq_D}{dt}$  and  $\ell_c$  the length of coil wire effectively subjected to the magnetic field  $B$ . This length depends on the coil position (phenomenon 1, see [2, figures 2.5–2.8] and [1, figure 5]). We propose a parametric plateau function  $\ell_c : q_D \mapsto \ell_c(q_D)$ :

$$\ell_c(q_D) = \ell_c^0 \frac{1 + \exp(-P_\ell)}{1 + \exp\left(P_\ell \left(\left(\frac{q_D}{Q_\ell}\right)^2 - 1\right)\right)}, \quad (8)$$

where  $\ell_c^0$  is the total length of the coil,  $Q_\ell$  describes the overhang of the coil with respect to the magnetic path (see figure 5a and [1, § 3.1.2]), and  $P_\ell$  is a shape parameter (see figure 5b).

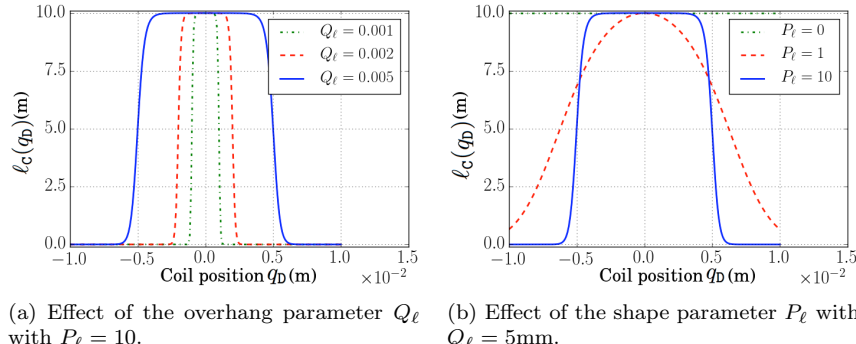


Figure 5: Effective length of coil wire  $\ell_c$  subjected to the magnetic field  $B$  as defined in (8), with coil position  $q_D$  and total wire length  $\ell_c^0 = 10\text{m}$ . Notice  $P_\ell = 0$  corresponds to  $\ell_c = \ell_c^0$ .

*Port-Hamiltonian formulation.* The model 0 is recast as a port-Hamiltonian system (3) by rewriting the Thiele/Small model (1)–(2) for the above definitions:

$$\begin{aligned}\frac{dx_1}{dt} &= -B \ell_c(x_3) \frac{\partial H}{\partial x_2}(x_2) - z_1(w_1) + u_1, \\ \frac{dx_2}{dt} &= B \ell_c(x_3) \frac{\partial H}{\partial x_1}(x_1) - \frac{\partial H}{\partial x_3}(x_3) - z_2(w_2),\end{aligned}\quad (9)$$

with  $v_D = \frac{\partial H}{\partial x_2}(x_2) = \frac{dx_3}{dt} = w_2$  and  $i_c = \frac{\partial H}{\partial x_2}(x_2) = w_1 = y_1$ . The corresponding structure is given in table 3.

*Simulation results.* Simulation are performed with the passive-guaranteed numerical method associated with the pH structure (3) recalled in Appendix A. Results are shown in figure 6 for different values of the overhang parameter  $Q_\ell$ . We see the symmetrical relation assumed for  $\ell_c(q_D)$  induces a doubling period in the force factor. Notice the (numerical) power balance is satisfied.

State: $\mathbf{x} = (\phi_c, p_M, q_D)^\top$	Energy: $H(\mathbf{x}) = \frac{x_1^2}{2L_c} + \frac{x_2^2}{2M_{CD}} + K_{SA} \frac{x_3^2}{2}$
Dissipation variable: $\mathbf{w} = (i_c, \frac{dq_D}{dt})^\top$	Dissipation law: $\mathbf{z}(\mathbf{w}) = \text{diag}(R_c, R_{SA}) \mathbf{w}$
Input: $\mathbf{u} = (v_I)^\top$	Output: $\mathbf{y} = (i_c)^\top$
Structure: $\mathbf{J}_x = \begin{pmatrix} 0 & -B\ell_c(x_3) & 0 \\ B\ell_c(x_3) & 0 & -1 \\ 0 & 1 & 0 \end{pmatrix}, \mathbf{K} = \begin{pmatrix} 1 & 0 \\ 0 & 1 \\ 0 & 0 \end{pmatrix},$ $\mathbf{G}_x = (1, 0, 0)^\top, \mathbf{J}_w = \mathbb{0}_{2 \times 2}, \mathbf{G}_w = \mathbb{0}_{2 \times 1}, \mathbf{J}_y = 0.$	

Table 3: Port-Hamiltonian formulation (3) for the Thiele/Small structure with position-dependent force factor (model 0) as depicted in figure 4, with magnetic flux in the coil  $\phi_c$ , diaphragm position  $q_D$  and momentum  $p_M = M_{CD} \frac{dq_D}{dt}$ . The position-dependent effective wire length  $\ell_c(q_D)$  is defined in (8). Physical parameters are given in table E.11.

The model 0 in table 3 is refined in the sequel to cope with the phenomena listed in section 2.2.

#### 4. Refined mechanics (model 1)

In this section, the model 0 from section 3.3 is refined to cope with creep effect (phenomenon 4) and nonlinear stress-strain relation (phenomenon 5) attached to the suspension material (S). Firstly, we detail the modeling of the creep effect based on fractional calculus elements, which results in a linear port-Hamiltonian system. Secondly, the hardening suspension effect is included, and the resulting nonlinear system is replaced in model 0 to form the model 1. Thirdly, simulation results are shown.

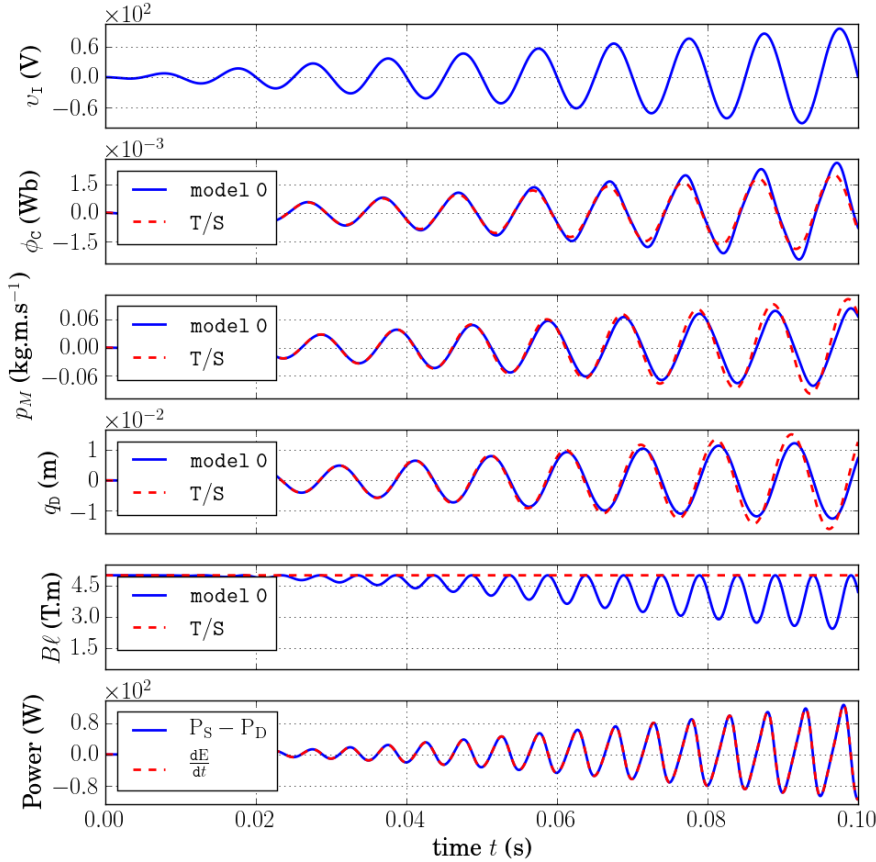
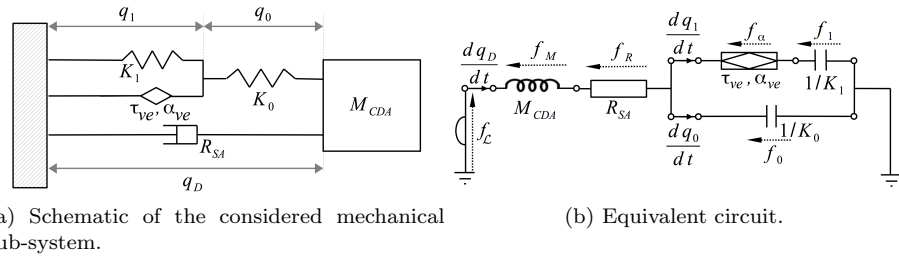


Figure 6: Simulation results for the model 0 in table 3. Physical parameters are given in table E.11. The input voltage  $v_I$  is a 100Hz sine wave with increasing amplitude between 0 and 50V. The sampling rate is  $F_s = 96\text{kHz}$ . The power balance is shown for the case  $P_\ell = 5$  only.

#### 4.1. Suspension creep

The creep effect is a long-term shape-memory of suspension material: when a step force is applied, first the diaphragm moves quite instantaneously to an equilibrium for which the restoring force is exactly compensating, and second a very slow displacement occurs, due to rearrangements in the crystal lattice of the material (see *e.g.* [28, figure 1] and [29, figure 11]). This phenomenon is enhanced by heat relaxation of the fluid in the enclosure [17]: when the volume of the container is put under pressure, the fluid's pressure rise in an adiabatic process to compensate the external pressure, and then decreases with cooling due to exchanges with the anisothermal boundaries.

Several modeling of the creep effect have been proposed in the frequency domain, among which the *exp-model* (fractional differentiator) in ([28, eq. (8)]), the *log-model* (frequency-dependent stiffness) in [28], *FDD-model* (frequency-dependent damping) in [17, 41]. The frequency domain approach is motivated by the fact that long-time memory effects can be appropriately described by fractional-order linear dynamics (see e.g. [42, 43, 44],[45][part 6] and reference therein for details). Here we consider the fractional extension of the Kelvin-Voigt modeling proposed in [42]. The resulting (linear) mechanical subsystem is depicted in figure 7 and is recast as a port-Hamiltonian system (3).



(a) Schematic of the considered mechanical sub-system. (b) Equivalent circuit.

Figure 7: Small-signal modeling of the mechanical part which includes: the total mass  $M_{CDA}$  (diaphragm, coil and additional mass due to acoustic radiation), the fluid-like damper  $R_{SA}$  (mechanical friction and small signal approximation for the acoustic power radiation), primary stiffness  $K_0$  and fractional Kelvin-Voigt modeling of the creep effect ( $K_1, \tau_{ve}, \alpha_{ve}$ ), with diaphragm position  $q_D$ , primary elongation  $q_0$ , creep elongation  $q_1$  and finite dimensional realization of the fractional differentiator in (15). Parameters are given in tables E.11 and E.12.

275

#### 4.1.1. Description of the creep model

Viscoelastic materials exhibit combination of elastic solids behaviors and viscous fluid behaviors. Let  $R$  be the coefficient of viscosity for a damper ( $\text{N.s.m}^{-1}$ ) and  $K$  the modulus of elasticity for a spring element ( $\text{N.m}^{-1}$ ) with characteristic frequency  $\omega_\alpha = \frac{K}{R}$  (Hz) and associated *creep time* is  $\tau_\alpha = \frac{2\pi}{\omega_\alpha}$  (s). The *fractional calculus element* defined in [42, (3.1)] restores a fractional order compliance in Laplace domain:  $\mathcal{T}_\alpha(s) = \frac{q_\alpha(s)}{f_\alpha(s)} = \frac{1}{K} \left( \frac{s}{\omega_\alpha} \right)^{\alpha-1}$  with  $s \in \mathbb{C}$  the Laplace variable,  $q_\alpha(s)$  the Laplace transform of element elongation and  $f_\alpha(s)$  the Laplace transform of the restoring force. The associated velocity  $v_\alpha(s) = s q_\alpha(s)$  is

$$v_\alpha(s) = \frac{1}{R} \left( \frac{s}{\omega_\alpha} \right)^\alpha f_\alpha(s). \quad (10)$$

that is, a fractional differentiator of order  $\alpha$ . Parameter  $\alpha$  can be regarded as a *memory parameter*: for  $\alpha = 0$ ,  $f_\alpha(s) = R v_\alpha(s)$  (no memory or algebraic relation) and for  $\alpha = 1$ ,  $f_\alpha(s) = K s^{-1} v_\alpha(s)$  (perfect memory or integrator). The *fractional calculus Kelvin-Voigt* modeling of the creep effect [42, § 4] is constructed by connecting a linear spring with same stiffness  $K$  in parallel to a fractional calculus element (10). The elongation is the same for both elements

$q_{\text{kv}} = q_\alpha$  and forces sum up  $f_{\text{kv}} = f_\alpha + K q_\alpha$ . The corresponding compliance is

$$\mathcal{T}_{\text{kv}}(s) = \frac{q_{\text{kv}}(s)}{f_{\text{kv}}(s)} = \left( K \left( 1 + \left( \frac{s}{\omega_\alpha} \right)^{1-\alpha} \right) \right)^{-1}. \quad (11)$$

The modeling of materials that exhibits several relaxation times  $\tau_n = \frac{2\pi}{\omega_n}$  is achieved by chaining  $N$  fractional calculus Kelvin-Voig elements (see [42, § 4], [46] and [47, figure 1]). Each element contributes to the total elongation  $q_{\text{chain}} = \sum_{n=1}^N q_n$ , and every elements experience the same force  $f_{\text{chain}} = f_1 = \dots = f_N$ . The total compliance is therefore

$$\mathcal{T}_{\text{chain}}(s) = \frac{s_{\text{chain}}(s)}{f_{\text{chain}}(s)} = \sum_{n=1}^N \left( K_n \left( 1 + \left( \frac{s}{\omega_n} \right)^{1-\alpha_n} \right) \right)^{-1}, \quad \omega_n = \frac{K_n}{R_n}. \quad (12)$$

Here, we consider the three elements fractional calculus solid model that restores (i) a primary instantaneous response to a step force with stiffness  $K_0$  and (ii) a long time viscoelastic memory with characteristic time  $\tau_{\text{ve}} = \frac{2\pi}{\omega_1}$ . The compliance of this viscoelastic model is

$$\mathcal{T}_{\text{ve}}(s) = \frac{1}{K_0} + \left( K_1 \left( 1 + \left( \frac{s}{\omega_1} \right)^{1-\alpha_{\text{ve}}} \right) \right)^{-1}; \quad \omega_1 = \frac{K_1}{R_1}. \quad (13)$$

Parameters  $K_0$  and  $K_1$  are related to  $K_{\text{SA}}$  according to

$$\begin{aligned} K_0 &= \frac{K_{\text{SA}}}{P_K} \\ K_1 &= \frac{K_{\text{SA}}}{2(1-P_K)} \end{aligned} \quad (14)$$

where parameter  $0 < P_K < 1$  describes the partition of  $K_{\text{SA}}$  between  $K_0$  and  $K_1$ , so that  $\mathcal{T}_{\text{ve}}(s)|_{\alpha_{\text{ve}}=1} = K_{\text{SA}} s^{-1}$  and  $K_0 = K_1 = \frac{3K_{\text{SA}}}{2}$  for  $P_K = \frac{3}{2}$ .

#### 4.1.2. Port-Hamiltonian formulation

The creep model (13) corresponds to the parallel connection of (i) a linear spring  $K_0$  and (ii) a linear spring  $K_1$  serially connected to a fractional calculus element (10) with stiffness  $K_1$ , characteristic frequency  $\omega_1 = \frac{2\pi}{\tau_{\text{ve}}}$  and memory parameter  $\alpha_{\text{ve}}$  (see figure 7). The port-Hamiltonian modeling of linear stiffness  $K_i$  with associated potential energy  $H_i(q_i) = \frac{K_i}{2}q_i^2$  has been addressed in section 3.2.

The port-Hamiltonian modeling of fractional calculus elements (10) has been addressed in [48]. First, an infinite dimensional state space formulation of the transfer function (10) with input  $f_\alpha(s)$  and output  $v_\alpha = v_1(s) = \frac{\omega_1}{K_1} \left( \frac{s}{\omega_1} \right)^\alpha f_\alpha(s)$  is build based on a continuous aggregation of linear damping according to the *diffusive representation* formalism (see AppendixD.2). Second, a finite order approximation is built based on the interconnection of a finite set of  $n_{\text{ve}}$  linear

damping associated with the poles  $(\xi_1, \dots, \xi_{n_{ve}})$ , as detailed in Appendix D.3. The resulting time-domain port-Hamiltonian formulation is

$$\begin{pmatrix} \frac{d\mathbf{x}_{ve}}{dt} \\ \mathbf{w}_{ve} \\ v_1 \end{pmatrix} = \begin{pmatrix} \mathbb{0}_{n_{ve} \times n_{ve}} & -\text{diag}(\hat{\boldsymbol{\mu}}_{ve})^{-1} & \mathbb{0}_{n_{ve} \times 1} \\ \text{diag}(\hat{\boldsymbol{\mu}}_{ve})^{-\top} & \mathbb{0}_{n_{ve} \times n_{ve}} & -\mathbb{1}_{n_{ve} \times 1} \\ \mathbb{0}_{1 \times n_{ve}} & \mathbb{1}_{1 \times n_{ve}} & 0 \end{pmatrix} \begin{pmatrix} \nabla H_{ve}(\mathbf{x}_{ve}) \\ \mathbf{z}_{ve}(\mathbf{w}_{ve}) \\ f_\alpha \end{pmatrix} \quad (15)$$

with state  $\mathbf{x}_{ve} = (x_1, \dots, x_{n_{ve}})^\top$ , dissipation variable  $\mathbf{w}_{ve} = (w_1, \dots, w_{n_{ve}})^\top$ , and  $H_{ve}(\mathbf{x}_{ve}) = \frac{1}{2} \mathbf{x}_{ve}^\top \text{diag}(P_1, \dots, P_{n_{ve}}) \mathbf{x}_{ve}$ ,  $\mathbf{z}_{ve}(\mathbf{w}_{ve}) = \text{diag}(R_1, \dots, R_{n_{ve}}) \mathbf{w}_{ve}$  with the weights  $\hat{\boldsymbol{\mu}}_{ve}$  obtained from the minimization (D.8) for the transfer function  $\mathcal{I}_{1-\alpha_{ve}}$  and

$$\begin{cases} P_n &= \frac{\omega_1^{1-\alpha_{ve}}}{K_1} [\hat{\boldsymbol{\mu}}_{ve}]_n \xi_n, \\ R_n &= P_n [\hat{\boldsymbol{\mu}}_{ve}]_n, \end{cases} \quad n \in (1, \dots, n_{ve}). \quad (16)$$

The mechanical subsystem depicted in figure 7 includes  $n_x = 3 + n_{ve}$  storage components (mass  $M_{CDA}$ , primary stiffness  $K_0$ , secondary stiffness  $K_1$  and  $n_{ve}$  stiffnesses associated with the fractional calculus element  $f_\alpha$ ),  $n_w = 1 + n_{ve}$  dissipative components (damper  $R_{SA}$  and  $n_{ve}$  dampers associated with the fractional calculus element  $f_\alpha$ ) and  $n_y = 1$  port (Lorentz force  $f_L$ ). The state  $\mathbf{x} = (p_M, q_0, q_1, \mathbf{x}_{ve}^\top)^\top$  consists of the mass momentum  $p_M = M_{CDA} q_D$ , the primary and secondary elongations  $q_0$  and  $q_1$  (respectively), and the states  $\mathbf{x}_{ve}$  associated with the fractional calculus in (15). The Hamiltonian is the sum of the kinetic energy  $H_M(x_1) = \frac{x_1^2}{2M_{CDA}}$ , the primary and secondary potential energies  $H_0(x_2) = K_0 \frac{x_2^2}{2}$  and  $H_1(x_3) = K_1 \frac{x_3^2}{2}$  (respectively), and the Hamiltonian  $H_{ve}(\mathbf{x}_{ve})$  associated with the fractional calculus in (15). The dissipation variable is  $\mathbf{w} = (\frac{dq_0}{dt}, \mathbf{w}_{ve}^\top)^\top$  with linear dissipation law  $\mathbf{z}(\mathbf{w}) = \text{diag}(R_{SA}, R_1, \dots, R_{n_{ve}}) \mathbf{w}$  for the  $R_n$  in (D.11). The input/output are  $\mathbf{u} = (f_L)^\top$  and  $\mathbf{y} = (v_D)^\top$ . For these definitions, the interconnection in figure 7 yields

$$\begin{aligned} \frac{dx_1}{dt} &= -\frac{\partial H}{\partial x_2}(x_2) - z_1(w_1) + u_1 \\ \frac{dx_2}{dt} &= \frac{\partial H}{\partial x_1}(x_1) - v_1 \\ \frac{dx_3}{dt} &= v_1 \end{aligned} \quad (17)$$

with  $v_1 = \mathbb{1}_{1 \times n_{ve}} \mathbf{z}_{ve}(\mathbf{w}_{ve})$  from (15). This system is recast as a port-Hamiltonian system (3) for the structure in table 4 and the parameters in table E.12.

#### 4.2. Suspension hardening and model 1

For large displacement, the suspension behaves like an hardening spring (phenomenon 5 and [18, 49]). This should occur for instantaneous displacements, so that only the primary stiffness  $K_0$  in table 4 is affected. Firstly, the mechanical subsystem from previous section is changed to cope with this phenomenon. Secondly, the resulting nonlinear mechanical part is included in loudspeaker model 0 to build the loudspeaker model 1.

State: $\mathbf{x} = (p_M, q_0, q_1, \mathbf{x}_{ve}^\top)^\top$	Energy: $H(\mathbf{x}) = \mathbf{x}^\top \mathbf{Q} \mathbf{x}$
Dissipation variable: $\mathbf{w} = (v_D, \mathbf{w}_{ve}^\top)^\top$	Dissipation law: $\mathbf{z}(\mathbf{w}) = \mathbf{R} \mathbf{w}$
Input: $\mathbf{u} = (f_L)^\top$	Output: $\mathbf{y} = (v_D)^\top$
Structure: $\mathbf{J}_x = \begin{pmatrix} 0 & -1 & 0 & 0 \\ 1 & 0 & 0 & 0 \\ 0 & 0 & 0 & 0 \\ 0 & 0 & 0 & 0 \end{pmatrix}, \mathbf{K} = \begin{pmatrix} 1 & 0 \\ 0 & \mathbb{1}_{1 \times n_{ve}} \\ 0 & -\mathbb{1}_{1 \times n_{ve}} \\ 0 & \text{diag}(\hat{\mu}_{SA})^{-1} \end{pmatrix},$ $\mathbf{G}_x = (1, 0, 0, 0)^\top, \mathbf{J}_w = \emptyset, \mathbf{G}_w = \emptyset, \mathbf{J}_y = 0.$	

Table 4: Port-Hamiltonian formulation (3) for the proposed small signal model of the mechanical part in figure 7 driven by the Lorentz force  $f_L$ , with diaphragm position  $q_0$ , momentum  $p_M = M_{CDA} \frac{dq_0}{dt}$ , primary elongation  $q_0$ , creep elongation  $q_1$  and finite dimensional realization of the fractional differentiator in (15). Parameters are given in tables E.11 and E.12, with  $\mathbf{Q} = \frac{1}{2} \text{diag}(\frac{1}{M_{CDA}}, K_0, K_1, P_1, \dots, P_{n_{ve}})$  and  $\mathbf{R} = \text{diag}(R_{SA}, R_1, \dots, R_{n_{ve}})$ .

#### 4.2.1. Model description

The primary stiffness  $K_0$  in table 4 is changed to a nonlinear spring that exhibits a phenomenological saturation for an instantaneous elongation  $q_0 = \pm q_{\text{sat}}$  (symmetric). The associated constitutive law (C.1–C.3) in Appendix C is

$$c_{SA}(q_0) = q_0 + \frac{4P_{\text{sat}}^S}{4-\pi} \left( \tan \left( \frac{\pi \cdot q_0}{2q_{\text{sat}}} \right) - \frac{\pi \cdot q_0}{2q_{\text{sat}}} \right) \quad (18)$$

which yields the restoring force  $f_0(q_0) = K_0 c_{SA}(q_0)$  for the initial stiffness  $K_0$ . It corresponds to the addition of a saturating term that does not contribute around the origin, thus preserving the meaning of parameter  $K_0$  (small signal behavior). The associated storage function (C.4–C.6) is

$$H_{\text{sat}}^{\text{SA}}(q_0) = K_0 \left( \frac{q_0^2}{2} - \frac{8P_{\text{sat}}^S q_{\text{sat}}}{\pi(4-\pi)} \left( \ln \left| \cos \left( \frac{\pi q_0}{2q_{\text{sat}}} \right) \right| + \frac{1}{2} \left( \frac{\pi q_0}{2q_{\text{sat}}} \right)^2 \right) \right) \geq 0. \quad (19)$$

#### 4.2.2. Port-Hamiltonian formulation of Model 1

The port-Hamiltonian formulation of the loudspeaker model 1 that includes creep effect (phenomenon 4) and hardening suspension (phenomenon 5) is obtained by (i) replacing the potential energy  $K_0 \frac{q_0^2}{2}$  in table 4 by the nonlinear storage function (19) and (ii) connecting the mechanical port  $f_L$  to the RL circuit describing the electromagnetic part as in section 2.1. This results in the structure given in table 5 with parameters in table E.12.

#### 4.3. Simulation results

The simulations of model 1 are performed according to the structure preserving numerical method in Appendix A. Physical parameters are given in table E.11

State: $\mathbf{x} = (\phi_c, p_M, q_0, q_1, \mathbf{x}_{ve}^\top)^\top$	Energy: $H(\mathbf{x}) = \mathbf{x}^\top \mathbf{Q} \mathbf{x} + H_{sat}^{SA}(x_3)$
Dissipation variable: $\mathbf{w} = (v_D, \mathbf{w}_{ve}^\top)^\top$	Dissipation law: $\mathbf{z}(\mathbf{w}) = \mathbf{R} \mathbf{w}$
Input: $\mathbf{u} = (v_I)^\top$	Output: $\mathbf{y} = (i_c)^\top$
$\mathbf{J}_x = \begin{pmatrix} 0 & -B\ell_c(q_D) & 0 & 0 & 0 \\ B\ell_c(q_D)0 & 0 & -1 & 0 & 0 \\ 0 & 1 & 0 & 0 & 0 \\ 0 & 0 & 0 & 0 & 0 \\ 0 & 0 & 0 & 0 & 0 \end{pmatrix}, \mathbf{G}_x = \begin{pmatrix} 1 \\ 0 \\ 0 \\ 0 \\ 0 \end{pmatrix},$ $\mathbf{K} = \begin{pmatrix} 1 & 0 & 0 \\ 0 & 1 & 0 \\ 0 & 0 & -1 \\ 0 & 0 & 1 \\ 0 & 0 & \text{diag}(\hat{\mu}_{SA})^{-1} \end{pmatrix}, \mathbf{J}_w = \emptyset, \mathbf{G}_w = \emptyset, \mathbf{J}_y = 0.$	Structure:

Table 5: Port-Hamiltonian formulation (3) for the model 1 depicted in figure 10. The linear stiffness  $K_{SA}$  is replaced by fractional Kelvin-Voigt modeling of the creep effect from section 4.1 in serial connection with the nonlinear spring described in section 4.2, with diaphragm position  $q_D$ , momentum  $p_M = M_{CDA} \frac{dq}{dt}$ , primary elongation  $q_0$ , creep elongation  $q_1$  and finite dimensional realization of the fractional differentiator in (15). The nonlinear potential energy  $H_{sat}^{SA}(q_0)$  is given in (19). Parameters are given in tables E.11 and E.12, with  $\mathbf{Q} = \frac{1}{2} \text{diag}(\frac{1}{L_c}, \frac{1}{M_{CDA}}, 0, K_1, P_1, \dots, P_{n_{ve}})$  and  $\mathbf{R} = \text{diag}(R_c, R_{SA}, R_1, \dots, R_{n_{ve}})$ .

and E.12.

*Creep effect (Phenomenon 4).* The viscoelastic behavior of the suspension material results in a frequency-dependent compliance, *i.e.* the suspension at low frequencies appears to be softer than predicted by the Thiele/Small model (see e.g. [17, figure 12]). The proposed fractional order dynamics permits to recover this effect as shown in figure 9 and F.22 (left). The corresponding long time memory depicted in figures 9 and F.22 (right) proves in accordance with measurements in *e.g.* [28, figure 1] and [29, figure 11].

*Nonlinear suspension (Phenomenon 5).* The hardening effect associated with the nonlinear stress-strain characteristic of the suspension material is clearly visible in figure 10 where the primary elongation is reduced for higher value of shape parameter  $P_{sat}^S$ . This reduces the total displacement  $q_D$  and momentum  $p_M = M_{CDA} \frac{dq_D}{dt}$ , while the creep elongation is almost unchanged. Notice the power balanced is fulfilled with  $\frac{dE}{dt} = P_S - P_D$ .

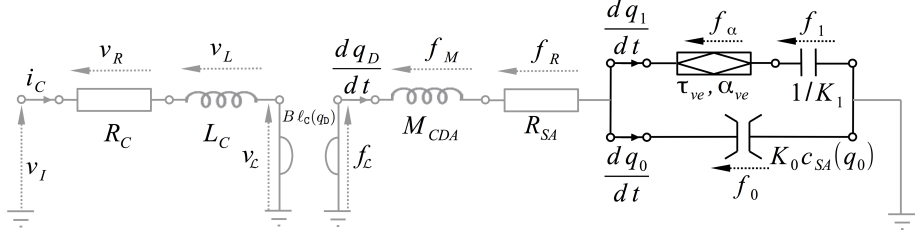


Figure 8: Equivalent circuit of the model 1 with diaphragm position  $q_D$ , primary elongation  $q_0$  and creep elongation  $q_1$ . Elements common to model 0 in figure 4 are shaded. The linear stiffness  $K_{SA}$  is replaced by (i) a fractional Kelvin-Voigt modeling of the viscoelastic phenomena with creep time  $\tau_{ve}$  and memory parameter  $\alpha_{ve}$  (see section 4.1) and (ii) a nonlinear element that restores the hardening of the suspension with constitutive law  $K_0 c_{SA}(q_0)$  given in (18) (see section 4.2).

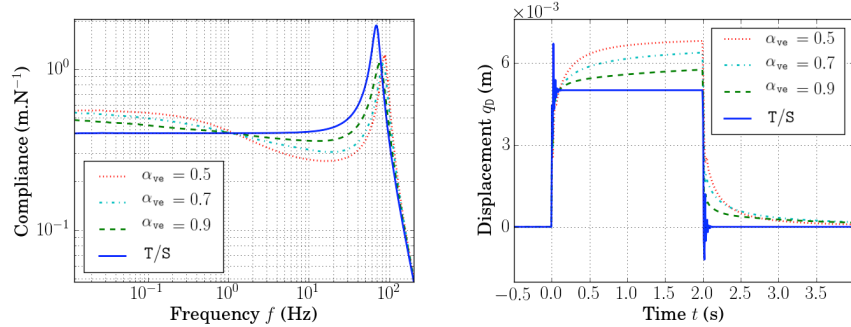


Figure 9: Simulation of the small-signal modeling of the mechanical subsystem in table 4 depicted in figure 7 with the parameters in tables E.11 and E.12 (except the memory parameter  $\alpha_{ve}$  indicated in the legend). Left: diaphragm displacement in response to the Lorentz force  $\left| \frac{q_0}{f_L} \right| (2i\pi f)$  (frequency domain). Right: diaphragm displacement in response to a 10N Lorentz force step between 0s and 2s (time domain). Legend T/S refers to the mechanical subsystem of the Thiele/Small modeling. Results for the creep time  $\tau_{ve}$  and partition parameter  $P_K$  are given in figure F.22. Sample rate is 10kHz.

## 5. Refined electromagnetic (model 2)

In this section, the Thiele/Small modeling is refined to account for effects of flux modulation (phenomenon 2), electromagnetic coupling (phenomenon 3), ferromagnetic saturation (phenomenon 6) and eddy currents (phenomenon 7) attached to the electromagnetic part (voice-coil C, magnet M, ferromagnetic path P and air gap G). Firstly, the proposed modeling is described. Secondly, this model is recast as a port-Hamiltonian system. Thirdly, simulation results are presented.

### 5.1. Model description

The classical lumped elements modeling of loudspeakers electrical impedance consists of the electrical DC resistance of the wire  $R_C$  serially connected to a non-

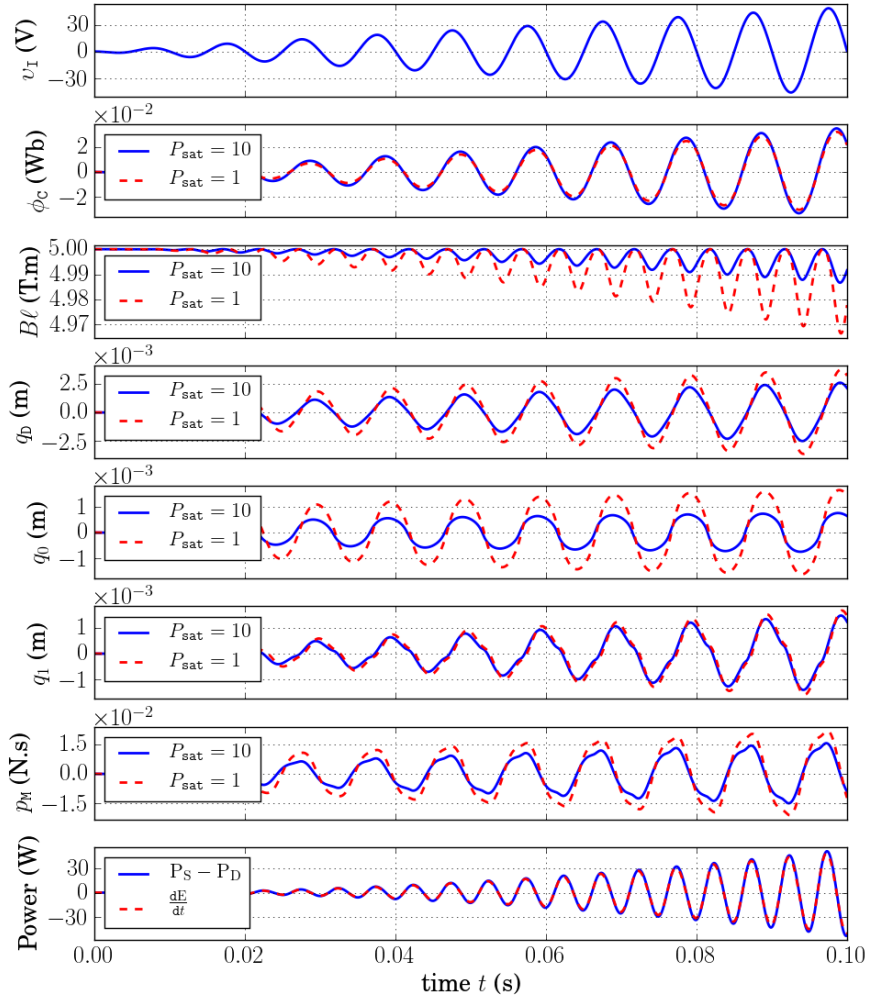


Figure 10: Simulation of the model 1 in table 5 depicted in figure 10, for the parameters in tables E.11 and E.12 (except  $P_{\text{sat}}^S$  indicated in the legend). The input voltage is a 100Hz sine wave with increasing amplitude between 0V and 50V. The sampling rate  $f_s = 96\text{kHz}$ . The power balance is shown for  $P_{\text{sat}}^S = 10$  only. Notice  $q_0 = q_0 + q_1$ .

standard inductive effect, referred as *lossy-inductor*. The simplest refinement of the Thiele/Small modeling is the *LR-2 model*, which uses a series inductor connected to a second inductor shunted by resistor. This structure has been refined by several authors [50, 51, 52, 16, 53] by considering nonstandard components instead of the ideal resistances and inductances to recover the measured electrical impedance. A frequency-dependent inductance has been considered in [50]. A weighted power functions of the frequency for both the real and imaginary part of the impedance is proposed in [51, 14].

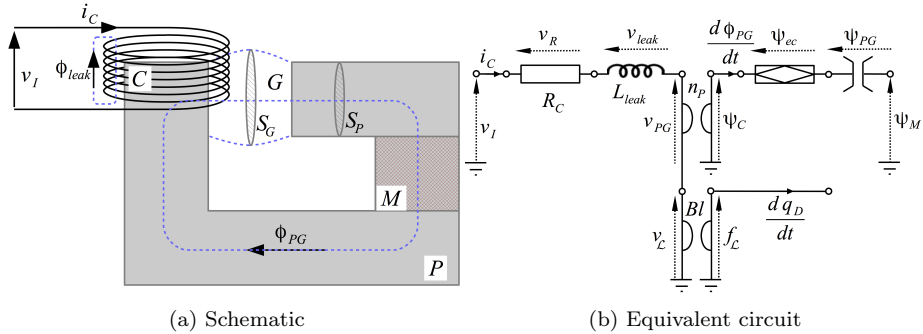


Figure 11: Simplified modeling of the electromagnetic circuit, which includes: the coil wire resistance  $R_C$ , the linear inductance associated with the leakage flux  $\phi_{\text{leak}}$ , the electromagnetic transduction with  $n_p$  the number of wire turns around the magnetic path, the magnetic energy storage in the ferromagnetic path described by the nonlinear induction-excitation curve  $\psi_{PG} \equiv \psi_{PG}(\phi_{PG})$  from (22), the fractional dynamics associated with eddy currents in the pole piece form (33), and the constant source of magnetomotive force  $\psi_M$  due to the magnet from (24).

340

The proposed modeling of the loudspeakers electrical impedance is depicted in figure 11. The coil winding acts as an electromagnetic transducer (gyrator) that realizes a coupling between the electrical and the magnetic domains, according to the gyrator-capacitor approach (see [54, 55] and recalls in AppendixB.3). The electrical domain includes the linear resistance  $R_C$  of the coil wire (same as Thiele/Small model) and a constant linear inductance associated with the magnetic flux that does not penetrate the pole piece (P). The flux in the magnetic path is common to (i) a nonlinear magnetic capacitor associated with energy storage in air gap (G, linear) and ferromagnetic (P, nonlinear), (ii) a fractional order differentiator associated with frequency-dependent losses (eddy currents) and (iii) a constant source of magnetomotive force associated with the permanent magnet (Ampère model).

345

350

### 5.1.1. Coil model

*Leakage inductance.* A single leakage flux  $\phi_{\text{leak}} = S_{\text{leak}} b_{\text{leak}}$  independent position  $q_D$  is assumed for every of the  $N_C$  wire turns (see 11a), with  $S_{\text{leak}}$  the average of the coil section and the inner annular surface between the coil and the pole piece. According to (B.1), the linear magnetic capacity of the air path

is  $C_{\text{leak}} = \frac{S_{\text{leak}} \mu_0 (1 + \xi_{\text{air}})}{2 A_c}$  with  $A_c$  the height of the coil wire turns,  $\mu_0$  the magnetic permeability of vacuum and  $\xi_{\text{air}}$  the magnetic susceptibility of air. From 360 (B.5), this corresponds to an electrical inductance with state  $x_{\text{leak}} = N_c \phi_{\text{leak}}$  and storage function  $H_{\text{leak}}(x_{\text{leak}}) = \frac{x_{\text{leak}}^2}{2 L_{\text{leak}}}$ , for the inductance  $L_{\text{leak}} = N_c^2 C_{\text{leak}}$ . Additionally, we define the characteristic frequency  $\omega_c = \frac{L_{\text{leak}}}{R_c}$  associated with the connection of  $L_{\text{leak}}$  with  $R_c$ .

*Electromagnetic coupling modulation.* The electromagnetic coupling between the coil (C) and the path (P) depends on the number  $n_p$  of wire turns effectively surrounding the pole piece. For small negative excursions  $q_D < 0$  every wire turns participate to the coupling  $n_p \sim N_c$ , and for large positive excursions the coil leaves the pole piece  $n_p \sim 0$ . We choose a phenomenological sigmoid relation  $n_p : q_D \mapsto n_p(q_D)$ :

$$n_p(q_D) = N_c \left( 1 + \exp \left( \frac{4 q_D - 2 (q_- + q_+)}{q_+ - q_-} \right) \right)^{-1} \quad (20)$$

with  $n_p(q_-) \simeq 90\% N_c$  and  $n_p(q_+) \simeq 10\% N_c$  (see figure 13). Some example are 365 depicted in figure 13a.

### 5.1.2. Ferromagnetic saturation

*Nonlinear storage.* The storage of magnetic energy in the magnetic circuit is spread over the pole piece (P) and the air gap (G). Assuming no leakage flux in the pole piece, those elements are crossed by the same magnetic flux  $\phi_{PG}$  (see figure 11a and [54, 55]). The corresponding averaged inductions are

$$\begin{aligned} b_P &= \frac{\phi_{PG}}{S_p}, \\ b_G &= \frac{\phi_{PG}}{S_g}, \end{aligned} \quad (21)$$

with  $S_p$  the average section crossed by the magnetic flux in the pole piece and  $S_g$  the section of the flux in the air gap (see figure 11a). This corresponds to the serial connection of two magnetic capacitors: the first one is associated with the air gap G with linear constitutive law (as for the leakage flux  $\phi_{\text{leak}}$ ); the second one is associated with the pole piece P and cannot be described by a linear magnetic capacity due to the magnetic saturation that occurs in ferromagnetic material (phenomenon 6). Those two serially-connected magnetic capacitors can merge into a single nonlinear capacitor which restores the total magnetomotive force  $\psi_{PG}(\phi_{PG})$ . We consider the tangent-like constitutive relation in AppendixC with flux saturation  $\phi_{\text{sat}} = S_p b_{\text{sat}}$ , where  $b_{\text{sat}}$  depends on the specific magnetic material. From (C.1–C.3), the constitutive law  $\psi_{PG}(\phi_{PG}) = c_{PG}(\phi_{PG})$  is

$$c_{PG}(\phi_{PG}) = P_{\text{lin}}^{PG} \left( \phi_{PG} + \frac{4 P_{\text{sat}}^{PG}}{4 - \pi} \left( \tan \left( \frac{\pi \phi_{PG}}{2 \phi_{\text{sat}}} \right) - \frac{\pi \phi_{PG}}{2 \phi_{\text{sat}}} \right) \right) \right) \quad (22)$$

where coefficient  $P_{\text{lin}}^{PG}$  includes the contributions of both air and pole piece material, and  $P_{\text{sat}}^{PG}$  is a shape parameter that depends on the specific material used

for the pole piece. The associated storage function (C.4–C.6) is

$$H_{\text{sat}}^{\text{PG}}(\phi_{\text{PG}}) = P_{\text{lin}}^{\text{PG}} \left( \frac{\phi_{\text{PG}}^2}{2} - \frac{8P_{\text{sat}}^{\text{PG}} \phi_{\text{sat}}}{\pi(4-\pi)} \left( \ln \left| \cos \left( \frac{\pi \phi_{\text{PG}}}{2\phi_{\text{sat}}} \right) \right| + \frac{1}{2} \left( \frac{\pi \phi_{\text{PG}}}{2\phi_{\text{sat}}} \right)^2 \right) \right) \geq 0. \quad (23)$$

*Steady state behavior.* The permanent magnet is modeled as a constant source of magnetomotive force  $\psi_{\text{M}}$  (Ampère model [55]). This drives the magnetic flux in the path to an equilibrium (steady-state)  $\phi_{\text{PG}} = \phi_{\text{ss}}$  for which the magnetomotive force exactly compensates that of the magnet:

$$\psi_{\text{PG}}(\phi_{\text{ss}}) = \psi_{\text{M}}. \quad (24)$$

The associated steady-state magnetic capacity is the inverse of the linear approximation of  $\psi_{\text{PG}}(\phi_{\text{PG}})$  around  $\phi_{\text{ss}}$ :

$$C_{\text{ss}} = \left( \frac{\partial c_{\text{PG}}}{\partial \phi_{\text{PG}}} (\phi_{\text{PG}} = \phi_{\text{ss}}) \right)^{-1} = \left( \frac{\partial^2 H_{\text{sat}}^{\text{PG}}}{\partial \phi_{\text{PG}}^2} (\phi_{\text{PG}} = \phi_{\text{ss}}) \right)^{-1}, \quad (25)$$

with  $\frac{\partial^2 H_{\text{sat}}^{\text{PG}}}{\partial \phi_{\text{PG}}^2} (\phi_{\text{PG}}) = P_{\text{lin}}^{\text{PG}} \left( 1 + \frac{2\pi P_{\text{sat}}^{\text{PG}}}{(\pi-4)\phi_{\text{sat}}} \left( 1 - \cos^{-2} \left( \frac{\pi \phi_{\text{PG}}}{2\phi_{\text{sat}}} \right) \right) \right)$ , so that  $P_{\text{lin}}^{\text{PG}}$  can be tuned according to

$$P_{\text{lin}}^{\text{PG}}(\phi_{\text{ss}}, \phi_{\text{sat}}, P_{\text{sat}}^{\text{PG}}, C_{\text{ss}}) = \frac{(\pi-4)\phi_{\text{sat}}}{C_{\text{ss}} \left( 2\pi P_{\text{sat}}^{\text{PG}} \left( 1 - \cos^{-2} \left( \frac{\pi \phi_{\text{ss}}}{2\phi_{\text{sat}}} \right) \right) + (\pi-4)\phi_{\text{sat}} \right)}. \quad (26)$$

### 5.1.3. Frequency-dependent losses

Besides the magnetic saturation, the pole piece is affected by the combination of capacitive and resistive effects due to eddy currents, resulting in frequency-dependent losses (phenomenon 7).

*Eddy currents model.* In this paper, we consider a linear fractional order magnetic capacity as found in [56, 45, 57, 32, 58, 3] and [45][part 5]. The *magnetic resistance*  $R_{\text{ec}}$  ( $\Omega^{-1}$ ) and *magnetic capacitance*  $C_{\text{ec}}$  (H) associated with eddy currents are merged into the *magnetic impedance*

$$\mathcal{T}_{\text{ec}}(s) = \frac{\psi_{\text{ec}}(s)}{s \phi_{\text{ec}}(s)} = R_{\text{ec}} \left( \frac{s}{\omega_{\text{ec}}} \right)^{-\alpha_{\text{ec}}} = \left( C_{\text{ec}} \omega_{\text{ec}} \left( \frac{s}{\omega_{\text{ec}}} \right)^{\alpha_{\text{ec}}} \right)^{-1}. \quad (27)$$

with  $s \in \mathbb{C}$  the Laplace variable, and  $\omega_{\text{ec}} = (R_{\text{ec}} C_{\text{ec}})^{-1}$  the characteristic frequency. Parameter  $\alpha_{\text{ec}}$  can be regarded as a memory parameter:  $\mathcal{T}_{\text{ec}}(s)$  restores a pure resistor for  $\alpha_{\text{ec}} = 0$  (no memory), and a pure capacitor for  $\alpha_{\text{ec}} = 1$  (perfect memory or integrator) with characteristic time  $\tau_{\text{ec}} = \frac{2\pi}{\omega_{\text{ec}}}$ . Notice the modulus of  $\mathcal{T}_{\text{ec}}(\omega_{\text{ec}})$  is independent of  $\alpha_{\text{ec}}$  (same in the resistive case  $\alpha_{\text{ec}} = 0$  as the capacitive case  $\alpha_{\text{ec}} = 1$ ). This fractional calculus element is serially connected to the magnetic capacity described in 5.1.2 with  $\phi_{\text{ec}} = \phi_{\text{PG}}$ , which

corresponds to the structure depicted in figure 11b. The resulting electrical impedance  $\mathcal{T}_P(s) = \frac{v_p}{i_c}$  associated with the pole piece in the the coil is

$$\mathcal{T}_P(s) = \frac{v_p(s)}{i_c(s)} = N_c^2 \left( \frac{1}{C_{ec} \omega_{ec} \left( \frac{s}{\omega_{ec}} \right)^{\alpha_{ec}}} + \frac{1}{C_{ss}s} \right)^{-1}. \quad (28)$$

For  $\alpha_{ec} = 1$ , (28) restores a pure inductance:  $\mathcal{T}_P(s) = L_p s$  with  $L_p = N_c^2 \frac{C_{ec} C_{ss}}{C_{ec} + C_{ss}}$  and we define

$$\begin{aligned} C_{ss} &= \frac{L_p}{N_c^2 p_L} \\ C_{ec} &= \frac{L_p}{N_c^2 (1-p_L)}. \end{aligned} \quad (29)$$

Parameter  $0 < p_L < 1$  describes the partition of  $L_p$  between  $C_{ss}$  and  $C_{ec}$  so that  $|\mathcal{T}_P(i\omega_{PG}, \alpha_{ec} = 0)| = |\mathcal{T}_P(i\omega_{PG}, \alpha_{ec} = 1)|$ , with characteristic frequency

$$\omega_{PG} = \omega_{ec} \sqrt{\frac{1+p_L}{1-p_L}}. \quad (30)$$

*Blocked electrical impedance.* The current  $i_c$  is common to (i) the resistor  $R_c$ , (ii) the leakage inductance  $L_{leak}$ , and (iii) the impedance associated with the coil core  $\mathcal{T}_{PG}(s)$ . For a coil blocked in fixed position ( $q_D = \frac{dq_D}{dt} = 0 \Rightarrow v_L = 0$ ), the total steady-state electrical impedance  $\mathcal{T}_c(s) = \frac{v_c(s)}{i_c(s)}$  measured at the coil terminals is

$$\mathcal{T}_c(s) = R_c \left( 1 + \frac{s}{\omega_c} \left[ 1 + \frac{L_p \omega_c}{p_L R_c} \left( \frac{1}{1 + \frac{1-p_L}{p_L} \left( \sqrt{\frac{1-p_L}{1+p_L}} \frac{s}{\omega_{PG}}} \right)^{1-\alpha_{ec}}} \right) \right] \right). \quad (31)$$

The DC value is given by the resistance  $R_c$ . For extremely high frequency, the impedance is governed by the leakage inductance  $\mathcal{T}_c(i\omega) \xrightarrow{\omega \rightarrow \infty} R_c \left( 1 + \frac{i\omega}{\omega_c} \right)$ . In between, the impedance depends on  $L_p$  (standard),  $\alpha_{ec}$  (see figure 15),  $\tau_{PG} = \frac{2\pi}{\omega_{PG}}$  (see figure F.23a), and  $p_L$  (see figure F.23b).

### 375 5.2. Port-Hamiltonian formulation

The proposed loudspeaker modeling with refined electromagnetic phenomena (model 2) corresponds to the replacement of the inductance  $L_c$  in model 0 by the electromagnetic model described above (compare figures 4 and 14). It includes a linear RL circuit (same as the one discussed in §3.2.2) serially connected 380 to the gyrator associated with the core of the coil described in §5.1.1 with the nonstandard elements described in §5.1.2 (nonlinear storage) and §5.1.3 (fractional dynamics).

*Time domain Fractional dynamics.* The port-Hamiltonian modeling of the fractional calculus elements (27) has been addressed in [48]. First, an infinite dimensional state space formulation of the transfer function with input  $\psi_{ec}$  and

output  $s\phi_{PG}(s) = \left(C_{ec} \omega_{ec} \left(\frac{s}{\omega_{ec}}\right)^{\alpha_{ec}}\right) \psi_{ec}(s)$  is build based on a continuous aggregation of linear damping according to the *diffusive representation* formalism (see Appendix D). Second, a finite order approximation is built based on the interconnection of a finite set of  $n_{ec}$  linear damping associated with the poles  $(\xi_1, \dots, \xi_{n_{ec}})$ , as detailed in Appendix D.3. The resulting time-domain port-Hamiltonian formulation is

$$\begin{pmatrix} \frac{d\mathbf{x}_{ec}}{dt} \\ \mathbf{w}_{ec} \\ \frac{d\phi_{PG}}{dt} \end{pmatrix} = \begin{pmatrix} \mathbb{0}_{n_{ec} \times n_{ec}} & -\text{diag}(\hat{\mu}_{ec})^{-1} & \mathbb{0}_{n_{ec} \times 1} \\ \text{diag}(\hat{\mu}_{ec})^{-T} & \mathbb{0}_{n_{ec} \times n_{ec}} & -\mathbb{1}_{n_{ec} \times 1} \\ \mathbb{0}_{1 \times n_{ec}} & \mathbb{1}_{1 \times n_{ec}} & 0 \end{pmatrix} \begin{pmatrix} \nabla H_{ec}(\mathbf{x}_{ec}) \\ \mathbf{z}_{ec}(\mathbf{w}_{ec}) \\ \psi_{ec} \end{pmatrix} \quad (32)$$

with state  $\mathbf{x}_{ec} = (x_1, \dots, x_{n_{ec}})^T$ , dissipation variable  $\mathbf{w}_{ec} = (w_1, \dots, w_{n_{ec}})^T$ , and  $H_{ec}(\mathbf{x}_{ec}) = \frac{1}{2} \mathbf{x}_{ec}^T \text{diag}(P_1, \dots, P_{n_{ec}}) \mathbf{x}_{ec}$ ,  $\mathbf{z}_{ec}(\mathbf{w}_{ec}) = \text{diag}(R_1, \dots, R_{n_{ec}}) \mathbf{w}_{ec}$  with the weights  $\hat{\mu}_{ec}$  obtained from the minimization (D.8) for the transfer function  $\mathcal{I}_{1-\alpha_{ec}}$  and

$$\begin{cases} P_n &= C_{ec} \omega_{ec}^{1-\alpha_{ec}} [\hat{\mu}_{ec}]_n \xi_n, \\ R_n &= P_n [\hat{\mu}_{ec}]_n, \end{cases} \quad n \in (1, \dots, n_{ec}). \quad (33)$$

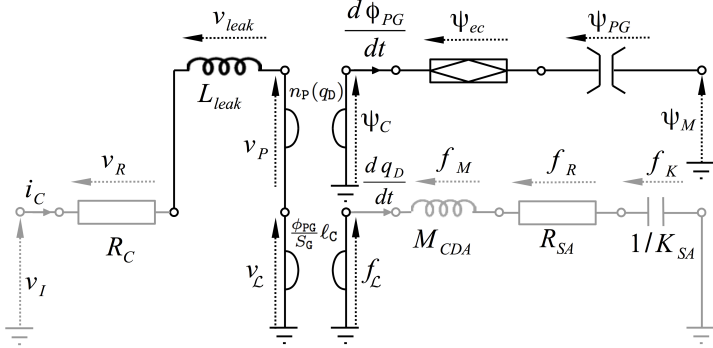


Figure 12: Equivalent circuit of the model 2 described in table 6. Elements common to model 0 in figure 4 are shaded. The coil inductance  $L_c$  is replaced by the electromagnetic circuit from figure 11b which include the leakage inductance  $L_{leak}$  and the explicit modeling of the magnetic path (pole piece P and air gap G). The latter includes (i) constant magnetomotive force due to the magnet  $\psi_M$  from (24), (ii) ferromagnetic saturation  $\psi_{PG}(\phi_{PG})$  from (22), (iii) fractional order dynamics associated with eddy currents from (33) and (27), and (iv) position-dependent electromagnetic coupling  $n_p(q_p)$  from (20). The induction is replaced by its actual value from (21):  $B = \frac{\phi_{PG}}{S_G}$ .

*Model 2.* The loudspeaker model 2 in figure 14 includes  $n_x = 4 + n_{ec}$  storage components (leakage inductance  $L_{leak}$ , nonlinear magnetic capacity  $c_{PG}$ , mass  $M_{CDA}$ , stiffness  $K_{SA}$  and  $n_{ec}$  linear capacitors associated with eddy currents),  $n_w = 2 + n_{ec}$  dissipative components (electrical resistance  $R_C$ , mechanical damping  $R_{SA}$  and  $n_{ec}$  resistors associated with eddy currents) and

$n_y = 2$  port (voltage  $v_I$  and constant magnetomotive force of the magnet  $\psi_M$ ). The state  $\mathbf{x} = (x_{\text{leak}}, \phi_{\text{PG}}, p_M, q_D, \mathbf{x}_{\text{ec}}^\top)^\top$  consists in the state associated with the leakage flux  $x_{\text{leak}} = N_c \phi_{\text{leak}}$ , the flux in the path  $\phi_{\text{PG}}$ , the mass momentum  $p_M = M_{\text{CDA}} \frac{dq_D}{dt}$ , the diaphragm position  $q_D$  and the states associated with eddy currents  $\mathbf{x}_{\text{ec}} = (x_1, \dots, x_{n_{\text{ec}}})^\top$ . The Hamiltonian of this system is  $H(\mathbf{x}) = \mathbf{x}^\top \mathbf{Q} \mathbf{x} + H_{\text{sat}}^{\text{PG}}(x_2)$  with  $\mathbf{Q} = \frac{1}{2} \text{diag}(\frac{1}{L_{\text{leak}}}, 0, \frac{1}{M_{\text{CDA}}}, K_{\text{SA}}, P_1, \dots, P_{n_{\text{ec}}})$  for the  $P_n$  in (33). The dissipation variable is  $\mathbf{w} = (i_C, \frac{dq_D}{dt}, \mathbf{w}_{\text{ec}}^\top)^\top$  with linear dissipation law  $\mathbf{z}(\mathbf{w}) = \text{diag}(R_C, R_{\text{SA}}, R_1, \dots, R_{n_{\text{ec}}}) \mathbf{w}$  for the  $R_n$  in (33). According to (21), the magnetic induction in the air gap involved in the electromechanical coupling (B.3) is  $b_G = \frac{\phi_{\text{PG}}}{S_g}$ . The length of wire effectively subjected to the induction field is  $\ell_C(x_4)$  given in (8). The number of wire turns effectively surrounding the pole piece involved in the electromagnetic coupling is  $n_P(x_4)$  given in (20). For these definitions, the dynamics is

$$\begin{aligned} \frac{dx_1}{dt} &= -\frac{x_2}{S_g} \ell_C(x_4) \frac{\partial H}{\partial x_3} - z_1(w_1) - n_P(x_4) \mathbb{1}_{1 \times n_{\text{ec}}} \mathbf{z}_{\text{ec}}(\mathbf{w}_{\text{ec}}) + u_1, \\ \frac{dx_3}{dt} &= \frac{x_2}{S_g} \ell_C(x_4) \frac{\partial H}{\partial x_1} - \frac{\partial H}{\partial x_4} - z_2(w_2), \\ \frac{d\mathbf{x}_{\text{ec}}}{dt} &= -\text{diag}(\hat{\boldsymbol{\mu}}_{\text{ec}})^{-1} \mathbf{z}_{\text{ec}}(\mathbf{w}_{\text{ec}}), \end{aligned} \quad (34)$$

with  $\frac{dx_2}{dt} = \mathbf{z}_{\text{ec}}(\mathbf{w}_{\text{ec}})$  and  $\frac{dx_4}{dt} = \frac{\partial H}{\partial x_3}$ . Finally, the port-Hamiltonian formulation (3) of the loudspeaker model 2, with refined electromagnetic part as depicted in figure 14, is given in table 6.

### 5.3. Simulation results

The simulations of model 2 are performed according to the structure preserving numerical method in Appendix A.

*Frequency-dependent losses (phenomenon 7).* Eddy currents result in frequency-dependent resistive effects: the slope at high frequencies is lower than predicted by the Theile/Small modeling. The fractional order dynamics permits to recover this phenomena as shown in figure 15b. The associated temporal evolution of the magnetic flux in the path is shown in figure 15a, where the long-term memory is clearly visible. Results for the partition parameter  $p_L$  and the characteristic time  $\tau_{\text{ec}} = \frac{2\pi}{\omega_{\text{PG}}}$  are given in figure F.23.

*Position-dependent electromagnetic coupling (phenomenon 3).* To illustrate the effect of coil position on the electrical impedance, the position  $q_D$  in model 2 (table 6) is fixed to -1cm (inside), 0cm (equilibrium) and +1cm (outside). Due to the position-dependent effective number of coil wire (20), this changes the inductance according to (B.5). Results are shown in figure 13b, in accordance with measurements in e.g. [1, figure 6].

*Core saturation (phenomenon 6).* The effect of the nonlinear magnetic behavior of the pole piece is illustrated by driving the system in steady states for which  $\phi_{\text{PG}} \neq \phi_{\text{ss}}$ , by imposing several DC voltages, here -100V, -10V, 10V and 100V (see evolution of flux  $\phi_{\text{PG}}$  in figure F.24b and current  $i_C$  in figure F.24a), with the blocked coil  $q_D = \frac{dq_D}{dt} = 0$ . Then, a small signal noise is applied to measure the

State: $\mathbf{x} = (x_{\text{leak}}, \phi_{\text{PG}}, p_{\text{M}}, q_{\text{D}}, \mathbf{x}_{\text{ec}}^{\top})^{\top}$	Energy: $H(\mathbf{x}) = \mathbf{x}^{\top} \mathbf{Q} \mathbf{x} + H_{\text{sat}}^{\text{PG}}(x_2)$
Dissipation variable: $\mathbf{w} = (i_{\text{C}}, \frac{dq_{\text{D}}}{dt}, \mathbf{w}_{\text{ec}}^{\top})^{\top}$	Dissipation law: $\mathbf{z}(\mathbf{w}) = \text{diag}(R_{\text{C}}, R_{\text{SA}}, R_1, \dots, R_{n_{\text{ec}}}) \mathbf{w}$
Input: $\mathbf{u} = (v_{\text{I}})^{\top}$	Output: $\mathbf{y} = (i_{\text{C}})^{\top}$
$\mathbf{J}_{\mathbf{x}} = \begin{pmatrix} 0 & 0 & -\frac{x_2}{S_{\text{G}}} \ell_{\text{C}}(x_4) & 0 & 0 \\ 0 & 0 & 0 & 0 & 0 \\ \frac{x_2}{S_{\text{G}}} \ell_{\text{C}}(x_4) & 0 & 0 & -1 & 0 \\ 0 & 0 & 1 & 0 & 0 \\ 0 & 0 & 0 & 0 & 0 \end{pmatrix}, \mathbf{G}_{\mathbf{x}} = \begin{pmatrix} 1 & 0 \\ 0 & 0 \\ 0 & 0 \\ 0 & 0 \\ 0 & 0 \end{pmatrix},$ $\mathbf{K} = \begin{pmatrix} 1 & 0 & n_{\text{P}}(x_4) \mathbb{1} \\ 0 & 0 & -\mathbb{1} \\ 0 & 1 & 0 \\ 0 & 0 & 0 \\ 0 & 0 & \text{diag}(\hat{\mu}_{\text{ec}})^{-1} \end{pmatrix}, \mathbf{G}_{\mathbf{w}} = \begin{pmatrix} 0 & 0 \\ 0 & 0 \\ 0 & -\mathbb{1} \end{pmatrix},$ $\mathbf{J}_{\mathbf{w}} = \emptyset, \mathbf{J}_{\mathbf{y}} = 0.$	

Table 6: Port-Hamiltonian formulation (3) for the loudspeaker model 2 discussed in §5.1 and depicted in figure 12, where the Lorentz force factor is the product of the magnetic induction in the air gap  $\phi_{\text{PG}}/S_{\text{G}}$  with the position-dependent effective wire length  $\ell_{\text{C}}(q_{\text{D}})$  defined in (8). Parameters are  $\mathbf{Q} = \frac{1}{2} \text{diag}(\frac{1}{L_{\text{leak}}}, 0, \frac{1}{M_{\text{CDA}}}, K_{\text{SA}}, P_1, \dots, P_{n_{\text{ec}}})$  and  $\mathbf{R} = \text{diag}(R_{\text{C}}, R_{\text{SA}}, R_1, \dots, R_{n_{\text{ec}}})$  for the definitions in tables E.13 and E.11 and in (33). The nonlinear storage function associated with the path PG is given in (23). The effective number of wire turns  $n_{\text{P}}(q_{\text{D}})$  involved in the electromagnetic coupling is given in (20).

resulting impedance. For medium DC values ( $\pm 10\text{V}$ ), the flux remains positive so that  $C_{\text{ss}}(v_{\text{DC}} = -10\text{V}) > C_{\text{ss}}(v_{\text{DC}} = 0\text{V}) > C_{\text{ss}}(v_{\text{DC}} = +10\text{V})$  (see figures 16a and F.24 and *e.g.* [1, figure 8]). For large negative DC value ( $-100\text{V}$ ), the magnetomotive force of the magnet is not sufficient to keep the flux in the pole piece positive (see F.24b). This yields  $C_{\text{ss}}(v_{\text{DC}} = +100\text{V}) < C_{\text{ss}}(v_{\text{DC}} = -100\text{V}) < C_{\text{ss}}(v_{\text{DC}} = 0\text{V})$  as shown in figure 16b.

*Flux-dependent force factor (phenomenon 2).* The force factor in model 2  $B_{\ell} \equiv \frac{\phi_{\text{PG}}}{S_{\text{G}}} \ell_{\text{C}}(q_{\text{D}})$  is modulated by the coil position (same as model 0) and the magnetic flux in the pole piece P and air gap G. This is clearly visible in the results of the figure 14, where we see the force factor can be larger than predicted by the Thiele/Small modeling. Notice the power balance is fulfilled.

## 6. Refined thermodynamics (model 3)

This section is devoted to the development of the loudspeaker model 3 that includes heating of coil wire due to Joule effect (phenomena 8 and 9). Thermodynamics behaviors are intrinsically *irreversible* phenomena, so that the *reversible*

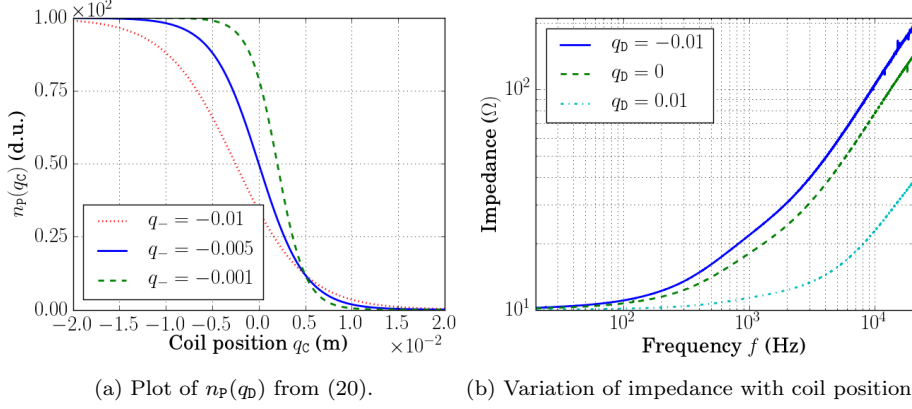


Figure 13: Effective number of wire turns involved in the electromagnetic coupling between the coil (C) with  $N_C = 100$  wire turns and the magnetic path (P), according to (20) for a maximal excursion  $q_+ = 5\text{mm}$  and incursions  $q_-$  mentioned in the legend. In figure 13b the coil is blocked in different positions, hence changing the number of coil wire turns around the path  $n_P(q_D)$  and thus the steady state inductance according to B.5.

port-Hamiltonian structure (3) has to be extended. We follow the approach in [59] to describes the entropy production associated with the conversion of dissipated power to thermal energy. Firstly, the heating and cooling phenomena are recast as irreversible port-Hamiltonian systems and the selected thermal modeling is presented. Secondly, the DC resistance  $R_C$  of the model 0 is replaced by the heating/cooling resistor. Thirdly, simulation results are presented.

### 6.1. Thermal modeling of the resistor

Firstly, the entropy production mechanism associated with the heating of the coil wire is described as an irreversible port-Hamiltonian system. Secondly, the thermal exchanges mechanism responsible for the cooling is described. Thirdly, we detail the selected thermal model that includes (i) heating of the wire, (ii) thermal exchanges with surrounding, and (iii) the increase of the resistivity with temperature.

#### 6.1.1. Entropy production

The first law of thermodynamics states that the change in the internal energy  $U$  of a closed<sup>2</sup> homogeneous system is  $dU = \delta Q - \delta W$ , where  $Q$  is the heat provided to the system and  $W$  the mechanical thermodynamic work performed by the system. The storage of thermal energy in a body is modeled as a simple thermal capacitance  $\delta Q = C d\theta$  where  $\theta > 0$  is the body's temperature, and

<sup>2</sup>A closed system does not exchange matter with its surrounding, but can exchange energy through its boundary.

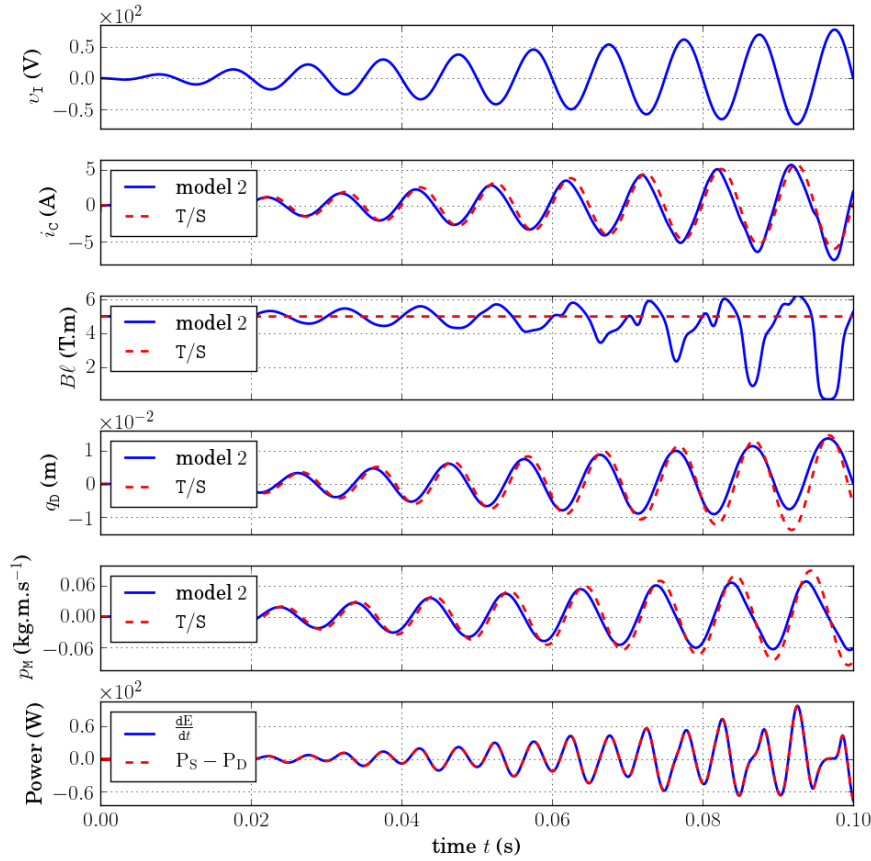
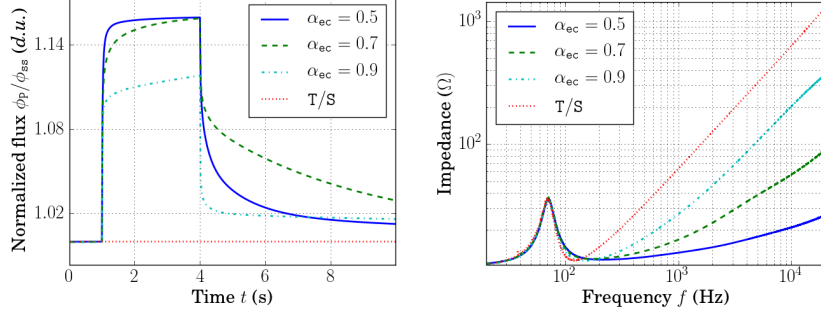
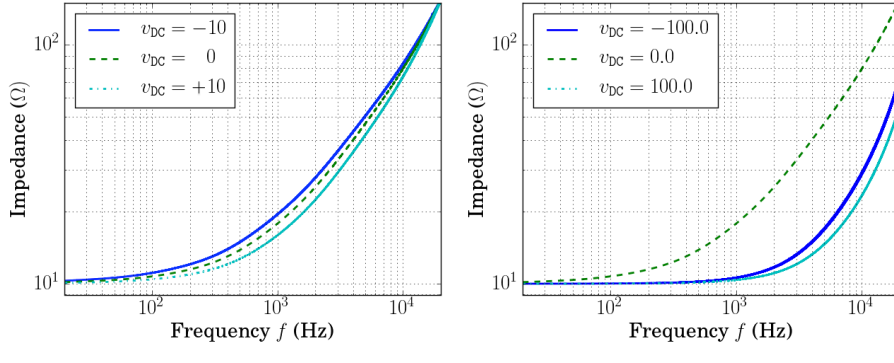


Figure 14: Simulation of the model 2 in table 6 depicted in figure 12, for the parameters in tables E.11 and E.13. The input voltage is a 100Hz sine wave with increasing amplitude between 0V and 80V. The sampling rate  $f_s = 96\text{kHz}$ . The power balance is shown for the model 2 only. The force factor  $B_\ell$  corresponds to the product of the induction in air gap  $b_g$  from (21) with position-dependent effective length from (8).



(a) Normalized flux  $\frac{\phi_p}{\phi_{ss}}$  in response to a 10V step voltage between 1s and 4s.  
(b) Modulus of impedance  $\left| \frac{v_I(2i\pi f)}{iC(2i\pi f)} \right|$ .

Figure 15: Simulation of the loudspeaker model 2 in table 6 and depicted in figure 14 with the parameters in tables E.11 and E.13 (except for the memory parameter indicated in the legend). Sample rate is 96kHz. Legend T/S refers to the Thiele/Small modeling. Results for the partition parameter  $p_L$  and the characteristic time  $\tau_{ec} = \frac{2\pi}{\omega_{pg}}$  are given in figure F.23.



(a) Blocked impedance,  $\pm 10$ V DC voltage      (b) Blocked impedance,  $\pm 100$ V DC voltage

Figure 16: Simulation of model 2 in table 6 and depicted in figure 14. The sampling rate is 96kHz. The coil is blocked:  $q_D = \frac{dq_D}{dt} = 0$ . The input voltage is  $v_I(t) = v_{DC} + v_{noise}(t)$  with  $v_{noise}$  a random signal normalized to 1mV. The DC value drives the magnetic flux in the pole piece to a new steady state different from  $\phi_{ss}$  (see figure F.24b), thus changing the equivalent magnetic capacity  $C_{ss} = \left( \frac{\partial^2 H_p}{\partial \phi_p^2}(\phi_{ss}) \right)^{-1}$  according to (25), see details in figures F.24c and F.24c. The evolution of the current  $i_C$  for each DC value is given in figure F.24a.

$C = mc_p$  with  $m$  is the mass (kg) of the body and  $c_p$  the specific heat ( $J \text{ kg}^{-1}\text{K}^{-1}$ ) of the material. Assuming no variation of the body volume and no isochoric work yields  $\delta W = 0$ . In this case, the second law of thermodynamics states that  $d\sigma = \frac{\delta Q}{\theta}$  is a total differential known as *entropy*. Then the variation

of entropy between two temperatures  $\theta_0$  and  $\theta_1$  is  $\sigma_1 - \sigma_0 = \int_{\theta_0}^{\theta_1} \frac{C}{\theta} d\theta$ , that is  $\theta_1(\sigma_1) = \theta_0 \exp\left(\frac{\sigma_1}{C}\right)$ , where we fixed  $\sigma_0 = 0$ . Defining

$$U(\sigma) = C\theta_0 \exp\left(\frac{\sigma}{C}\right), \quad (35)$$

the time variation of the internal energy is  $\frac{dU}{dt} = \theta \frac{d\sigma}{dt}$  with temperature

$$\theta(\sigma) = \frac{\partial U(\sigma)}{\partial \sigma}. \quad (36)$$

For the heating resistor,  $\frac{dU}{dt}$  is given by the dissipated power  $P_D = z(w)w$  so that  $\frac{d\sigma}{dt} = \frac{z(w)w}{\theta}$ . Considering a current controlled model with input  $u = i = w$  and output  $y = v = z(w)$  yields the following *irreversible port-Hamiltonian system*:

$$\begin{pmatrix} \frac{d\sigma}{dt} \\ -y \end{pmatrix} = \frac{z(u)}{\theta} \underbrace{\begin{pmatrix} 0 & 1 \\ -1 & 0 \end{pmatrix}}_{J_\theta} \begin{pmatrix} \frac{\partial U}{\partial \sigma} \\ u \end{pmatrix}. \quad (37)$$

The skew-symmetry of  $J_\theta$  ensures the entire power lost from the electrical domain is converted to heat; the multiplying term  $\frac{z(u)}{\theta}$  ensures that the dissipated power is positive.

#### <sup>440</sup> 6.1.2. Heat transfers

The cooling of the resistor is due to thermal exchanges with the environment. The heat transfer between two bodies  $(\sigma_1, \theta_1)$  and  $(\sigma_2, \theta_2)$  is described as follows. From Newton's law of cooling, the heat flowing into body  $i$  due to the temperature gradient  $\Delta\theta_{j \rightarrow i} = \theta_j - \theta_i$  obeys  $\frac{\delta Q_i}{\delta t} = \frac{dU_i}{dt} = R_{12} \Delta\theta_{j \rightarrow i}$  for  $i, j = 1, 2$ , where  $R_{12}$  is the thermal resistance ( $\text{W.K}^{-1}$ ). This can be recast as the following irreversible port-Hamiltonian system:

$$\begin{pmatrix} \frac{d\sigma_1}{dt} \\ \frac{d\sigma_2}{dt} \end{pmatrix} = \begin{pmatrix} -\frac{R_{12}}{\theta_1} & +\frac{R_{12}}{\theta_1} \\ +\frac{R_{12}}{\theta_2} & -\frac{R_{12}}{\theta_2} \end{pmatrix} \begin{pmatrix} \frac{\partial U_1}{\partial \sigma_1} \\ \frac{\partial U_2}{\partial \sigma_2} \end{pmatrix}. \quad (38)$$

Notice the variation of total internal energy is  $\frac{dU}{dt} = \sum_{i=1}^2 \frac{\partial U_i}{\partial \sigma_i} \frac{d\sigma_i}{dt} = 0$  and the variation of total entropy is  $\frac{d\sigma}{dt} = \frac{d\sigma_1}{dt} + \frac{d\sigma_2}{dt} = R_{12} \frac{(\theta_1 - \theta_2)^2}{\theta_1 \theta_2} \geq 0$ .

#### 6.1.3. Thermal model

*Thermal element.* According to the third order thermal model of loudspeaker proposed in [13], we introduce the thermal quantities associated with the voice coil  $(\sigma_C, \theta_C, C_C)$ , the air gap  $(\sigma_A, \theta_A, C_A)$ , the pole piece  $(\sigma_P, \theta_P, C_P)$  and the air in enclosure  $(\sigma_E, \theta_E, C_E)$ . This model includes heat transfers of (i) the coil wire with the air gap  $R_{CG}$ , (ii) the air gap with the pole piece  $R_{GP}$ , and (iii) the pole piece with the air in enclosure  $R_{PE}$  (see figure 17).

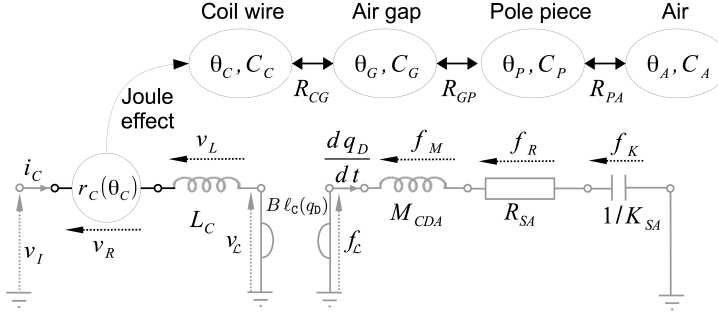


Figure 17: Synopsis of the thermal transfers in the third order modeling proposed in [13] and used in this paper. Temperatures of the coil wire, the air gap, the magnetic path and the ambient air are denoted by  $\theta_C$ ,  $\theta_G$ ,  $\theta_P$  and  $\theta_A$  respectively. Corresponding thermal capacitance are denoted by  $C_C$ ,  $C_G$ ,  $C_P$  and  $C_A$ . The thermal resistance that opposes to the heat transfer is  $R_{CG}$  between the coil and the air gap,  $R_{GP}$  between the air gap and the pole piece and  $R_{PA}$  between the pole piece and the air in enclosure. the temperature-dependent resistance  $r_C(\theta_C)$  is given in (39).

*Temperature-dependent resistance.* According to [33] (see also [15] and [13, (14)]), a simple model of wire resistance  $r_C(\theta_C)$  with the wire temperature  $\theta_C$  is

$$r_C(\theta_C) = R_C (1 + \alpha_\tau (\theta_C - \theta_0)), \quad (39)$$

where  $R_C$  the DC resistance of the coil measured at temperature  $\theta_0$ , and  $\alpha_\tau$  a temperature coefficient. Denoting  $i_C$  the current and  $v_R$  the tension associated with the resistive effect of the coil, this model is recast as an irreversible port-Hamiltonian system as follows:

$$\left( \begin{array}{c} \frac{d\sigma_C}{dt} \\ \frac{d\sigma_G}{dt} \\ \frac{d\sigma_P}{dt} \\ \frac{d\sigma_A}{dt} \\ -v_R \end{array} \right) = \left( \begin{array}{cc|c} -\frac{R_{CG}}{\theta_C} & \frac{R_{CG}}{\theta_C} & 0 & 0 & \frac{r_C(\theta_C) i_C}{\theta_C} \\ \frac{R_{CG}}{\theta_G} & -\frac{R_{CG}+R_{GP}}{\theta_G} & \frac{R_{GP}}{\theta_G} & 0 & 0 \\ 0 & \frac{R_{GP}}{\theta_P} & -\frac{R_{GP}+R_{PA}}{\theta_P} & \frac{R_{PA}}{\theta_P} & 0 \\ 0 & 0 & \frac{R_{PA}}{\theta_A} & -\frac{R_{PA}}{\theta_A} & 0 \\ -\frac{r_C(\theta_C) i_C}{\theta_C} & 0 & 0 & 0 & 0 \end{array} \right) \left( \begin{array}{c} \frac{\partial U_C}{\partial \sigma_C} \\ \frac{\partial U_G}{\partial \sigma_G} \\ \frac{\partial U_P}{\partial \sigma_P} \\ \frac{\partial U_A}{\partial \sigma_A} \\ i_C \end{array} \right) \quad (40)$$

## 450 6.2. Replacement in model 0

The replacement of the DC resistance  $R_C$  in the model 0 from section 2.1 by the thermal resistor model (40) is as follows. The system includes  $n_x = 7$  storage components (coil inductance  $L_C$ , mass  $M_{CDA}$ , stiffness  $K_{SA}$  and thermal capacitances  $C_C, C_G, C_P, C_A$ ),  $n_w = 1$  dissipative component (mechanical damping  $R_{SA}$ ) and  $n_y = 1$  port (electrical input  $v_I$ ). The state  $\mathbf{x} = (\phi_C, p_M, q_D, \sigma_C, \sigma_G, \sigma_P, \sigma_A)^\top$  consists of the magnetic flux in the coil  $\phi_C$ , mass momentum  $p_M = M_{CDA} \frac{dq_D}{dt}$ , diaphragm position  $q_D$  and collection of entropies. The Hamiltonian is the sum of the electrodynamic energy  $H_L(x_1) = \frac{x_1^2}{2L_C}$ , the kinetic energy  $H_M(x_2) = \frac{x_2^2}{2M_{CDA}}$ , the potential energy  $H_K(x_3) = \frac{x_3^2}{2K_{SA}}$  and thermal energies  $U_C, U_G, U_P, U_A$ . The

<sup>460</sup> dissipation variable is  $\mathbf{w} = \left(\frac{dq_D}{dt}\right)^\top$  with linear dissipation law  $\mathbf{z}(\mathbf{w}) = R_{SA} \mathbf{w}$ . As in section 2.1, the current in the wire is imposed by coil inductance  $i_C = \frac{\partial H_L}{\partial x_1} = \frac{x_1}{L_c}$ . The resulting port-Hamiltonian system is given in table 7 with the parameters in table E.14.

State: $\mathbf{x} = (\phi_C, p_M, q_D, \sigma_C, \sigma_G, \sigma_P, \sigma_A)^\top$	Energy: $H(\mathbf{x}) = \mathbf{x}^\top \mathbf{Q} \mathbf{x} + U(\mathbf{x})$
Dissipation variable: $\mathbf{w} = \left(\frac{dq_D}{dt}\right)^\top$	Dissipation law: $\mathbf{z}(\mathbf{w}) = R_{SA} \mathbf{w}$
Input: $\mathbf{u} = (v_I)^\top$	Output: $\mathbf{y} = (i_C)^\top$
$\mathbf{J}_x = \left( \begin{array}{ccc ccc} 0 & -B\ell_C(x_3) & 0 & -\frac{r_C(\theta_C)x_1}{\theta_C L_C} & 0 & 0 & 0 \\ B\ell_C(x_3) & 0 & -1 & 0 & 0 & 0 & 0 \\ 0 & 1 & 0 & 0 & 0 & 0 & 0 \\ \hline \frac{r_C(\theta_C)x_1}{\theta_C L_C} & 0 & 0 & -\frac{R_{CG}}{\theta_C} & \frac{R_{CG}}{\theta_C} & 0 & 0 \\ 0 & 0 & 0 & \frac{R_{CG}}{\theta_G} & -\frac{R_{CG}+R_{GP}}{\theta_G} & \frac{R_{GP}}{\theta_G} & 0 \\ 0 & 0 & 0 & 0 & \frac{R_{GP}}{\theta_P} & -\frac{R_{GP}+R_{PA}}{\theta_P} & \frac{R_{PA}}{\theta_P} \\ 0 & 0 & 0 & 0 & 0 & \frac{R_{PA}}{\theta_A} & -\frac{R_{PA}}{\theta_A} \end{array} \right),$ $\mathbf{K} = \begin{pmatrix} 0 \\ 1 \\ 0 \end{pmatrix}, \mathbf{G}_x = \begin{pmatrix} 1 \\ 0 \\ 0 \end{pmatrix}, \mathbf{J}_w = 0, \mathbf{G}_w = 0, \mathbf{J}_y = 0.$	Structure:

Table 7: Irreversible port-Hamiltonian formulation based on structure (3) for the loudspeaker model 3 depicted in figure 17. It includes the heating/cooling resistor from (40) with the temperature-dependent resistance  $r_C(\theta_C)$  defined in (39). The internal energy is  $U(\mathbf{x}) = U_C(x_4) + U_G(x_5) + U_P(x_6) + U_A(x_7)$  with the  $U_i(\sigma_i)$  defined in (35). The  $\theta_i$  are function of the  $\sigma_i$  as defined in (36). Physical parameters are given in tables E.11 and E.14, with  $\mathbf{Q} = \frac{1}{2} \text{diag} \left( \frac{1}{L_C}, \frac{1}{M_{CDA}}, K_{SA}, 0, 0, 0, 0 \right)$ . The position-dependent effective wire length  $\ell_C(q_D)$  is defined in (8).

### 6.3. Simulation results

<sup>465</sup> The simulations of model 3 are performed according to the structure preserving numerical method in Appendix A. The input voltage consists in several bursts of 200Hz sine wave with amplitude 50V. We present a short time simulation in figure 18 (2 bursts of 5 periods) and a long simulation in figure 19 (5 bursts of 4 minutes, separated by 1 minute of rest with 10 minutes cooling).

<sup>470</sup> *Heating of coil wire (phenomenon 8).* The heating of the coil wire is visible in figure 19, where we see a rise from ambient temperature  $\theta_0 = 20^\circ\text{C}$  to  $\theta_C(25\text{min}) \sim 150^\circ\text{C}$ . The decrease due to thermal exchanges is also visible, with a cooling down to  $\theta_C(35\text{min}) \sim 40^\circ\text{C}$ . Notice the power balance is fulfilled (figure 18), and it is 0 for the cooling period (figure 19), that is, the total energy is preserved. The dissipated power is due solely to the mechanical friction  $R_{SA}$ .

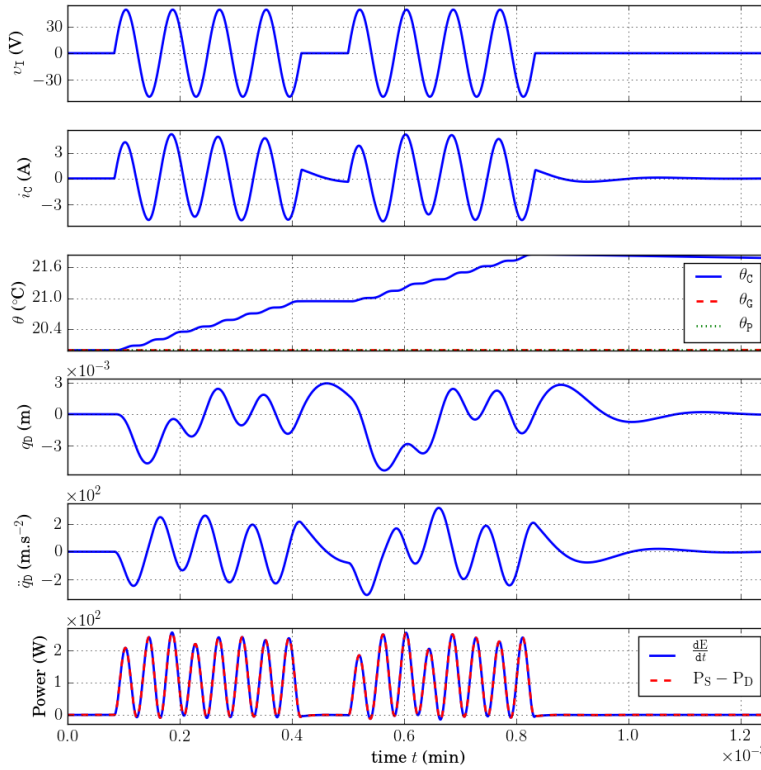


Figure 18: Short-time simulation of the model 3 in table 7 depicted in figure 17, for the parameters in tables E.11 and E.14. The input voltage is made of two bursts of four periods of a 200Hz sine wave with amplitude 50V. The sampling rate is 96kHz. Notice the increase in coil wire temperature  $\theta_c$ . The dissipated power is solely due to the friction damping  $R_{SA}$  (see table 7).

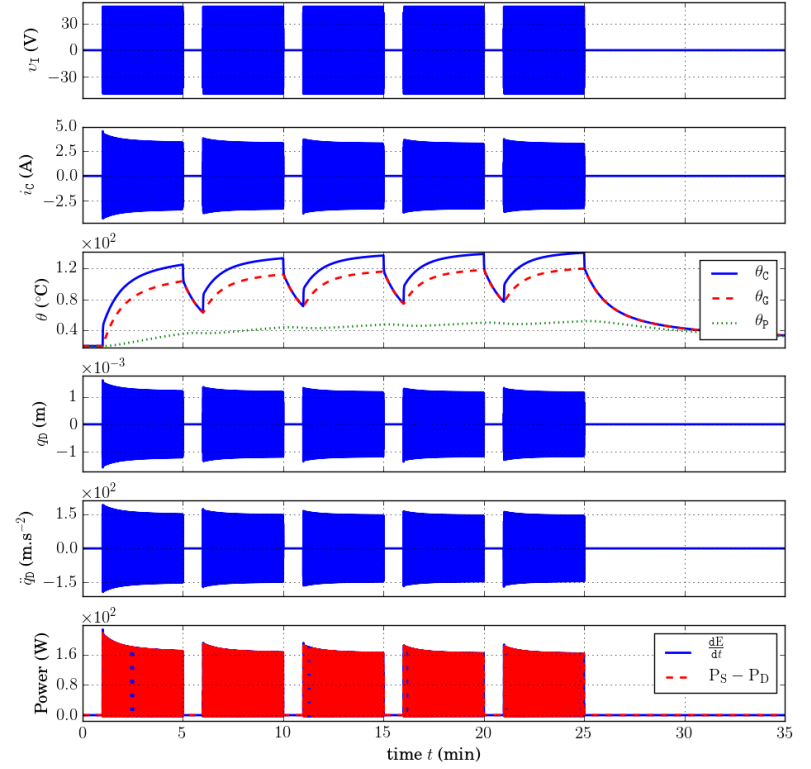


Figure 19: Long-time simulation of the model 3 in table 7 depicted in figure 17, for the parameters in tables E.11 and E.14. The input voltage is made of 5 bursts during 4 minutes of a 200Hz sine wave with amplitude 50V. The sampling rate is 96kHz. Notice the increase in coil wire temperature  $\theta_c$  and the compression due to the evolution of coil wire resistance  $r_c(\theta_c)$  in (39). The dissipated power is due solely to the friction damping  $R_{SA}$  (see table 7).

*Thermal compression (phenomenon 9).* The variation of the resistance  $r_c(\theta_c)$  from (39) is very low for the involved temperatures, due to the small temperature coefficient of copper  $\alpha_\tau = 4.10^{-3}\text{K}^{-1}$ . However, the compression of both the electrical and the mechanical signals is visible in figure 19.

## 480 7. Discussion

The three loudspeaker models 1, 2 and 3 have been developed independently of each other. This permits to illustrate the particular effect of each phenomenon on the loudspeaker dynamics. Now, their interconnection to form a global, multiphysical modeling that copes with all the phenomena described in section 2.2 is straightforward, due to the modularity of the port-Hamiltonian approach.

Phenomena	1	2	3	4	5	6	7	8	9
Model 0 §3.3	✓								
Model 1 §4	✓			✓	✓				
Model 2 §5	✓	✓	✓			✓	✓		
Model 3 §6	✓							✓	✓

Table 8: Phenomena in section 2.2 addressed by each port-Hamiltonian models.

485

## 8. Conclusion

In this paper, three lumped parameter models of the electrodynamic loudspeaker have been developed to cope with refined phenomena of (i) mechanical, (ii) electromagnetic and (iii) thermal origins. In particular, a finite dimensional time domain formulation of the fractional order dynamics associated with viscoelastic and eddy currents phenomena (linear) and material properties (stress-strain and b-h characteristics, nonlinear) have been derived. Those models are given in the framework of port-Hamiltonian systems, which decomposes the system into conservative, dissipative and source parts, also suitable for the thermal model. The numerical method used for the simulations preserves this decomposition as well as the power balance in the discrete time domain. Numerical results that comply with measurements from the literature have been presented.

500 The first perspective of this work is to achieve DSP simulation-based real-time audio distortion compensation, based on the preliminary work in [7]. This requires the development of a parameter estimation method dedicated to the port-Hamiltonian structure. A second perspective is to include detailed modeling of the acoustical load that is not addressed in this paper. Modal decomposition and Rayleigh integral methods [60, 61] are envisaged for this issue.

## 9. Acknowledgments

The authors acknowledge the members of the french National Research Agency project HaMecMoPSys for support in port-Hamiltonian theory, and Antonin Novak, Balbine Maillou (Laboratoire d'Acoustique de l'Université du Maine, UMR-CNRS 6613, Le Mans, France) and Pascal Brunet (Audio Group Samsung Research America, Los Angeles, United-States) for fruitful discussions on the loudspeaker mechanisms. Finally, the authors acknowledge Robert Piéchaud for taking the time to complete the proofread of this paper.

## References

- [1] W. Klippel, Tutorial: Loudspeaker nonlinearities causes, parameters, symptoms, *Journal of the Audio Engineering Society* 54 (10) (2006) 907–939.
- [2] B. R. Pedersen, Error correction of loudspeakers, Ph.D. thesis, PhD thesis. Aalborg University, Denmark (2008).
- [3] P. Brunet, Nonlinear system modeling and identification of loudspeakers, Ph.D. thesis, Northeastern University Boston (2014).
- [4] J. Suykens, J. Vandewalle, J. Van Ginderdeuren, Feedback linearization of nonlinear distortion in electrodynamic loudspeakers, *Journal of the audio engineering society* 43 (9) (1995) 690–694.
- [5] D. Jakobsson, M. Larsson, Modelling and compensation of nonlinear loudspeaker.
- [6] M. Arvidsson, D. Karlsson, Attenuation of harmonic distortion in loudspeakers using non-linear control.
- [7] A. Falaize, N. Papazoglou, T. Hélie, N. Lopes, Compensation of loudspeaker's nonlinearities based on flatness and port-Hamiltonian approach, in: 22ème Congrès Français de Mécanique, Association Française de Mécanique, Lyon, France, 2015.  
URL <https://hal.archives-ouvertes.fr/hal-01245632>
- [8] S. Tassart, S. Valcin, M. Menu, Active loudspeaker heat protection, *Journal of the Audio Engineering Society* 62 (11) (2014) 767–775.
- [9] N. Thiele, Loudspeakers in vented boxes: Part 1, *Journal of the Audio Engineering Society* 19 (5) (1971) 382–392.
- [10] N. Thiele, Loudspeakers in vented boxes: Part 2, *Journal of the Audio Engineering Society* 19 (6) (1971) 471–483.
- [11] R. H. Small, Closed-box loudspeaker systems-part 1: analysis, *Journal of the Audio Engineering Society* 20 (10) (1972) 798–808.

- [12] R. H. Small, Closed-box loudspeaker systems-part 2: Synthesis, *Journal of the Audio Engineering Society* 21 (1) (1973) 11–18.
- [13] P. J. Chapman, Thermal simulation of loudspeakers, in: *Audio Engineering Society Convention 104*, Audio Engineering Society, 1998.
- 545 [14] W. M. Leach Jr, Loudspeaker voice-coil inductance losses: circuit models, parameter estimation, and effect on frequency response, *Journal of the Audio Engineering Society* 50 (6) (2002) 442–450.
- [15] W. Klippel, Nonlinear modeling of the heat transfer in loudspeakers, *Journal of the Audio Engineering Society* 52 (1/2) (2004) 3–25.
- 550 [16] K. Thorborg, A. D. Unruh, C. J. Struck, An improved electrical equivalent circuit model for dynamic moving coil transducers, in: *Audio Engineering Society Convention*, Vol. 122, 2007.
- [17] K. Thorborg, C. Tinggaard, F. Agerkvist, C. Futtrup, Frequency dependence of damping and compliance in loudspeaker suspensions, *Journal of the Audio Engineering Society* 58 (6) (2010) 472–486.
- 555 [18] F. T. Agerkvist, Non-linear viscoelastic models, in: *Audio Engineering Society Convention 131*, Audio Engineering Society, 2011.
- [19] W. Klippel, Dynamic measurement and interpretation of the nonlinear parameters of electrodynamic loudspeakers, *Journal of the Audio Engineering Society* 38 (12) (1990) 944–955.
- 560 [20] M. R. Bai, C.-M. Huang, Expert diagnostic system for moving-coil loudspeakers using nonlinear modeling, *The Journal of the Acoustical Society of America* 125 (2) (2009) 819–830.
- 565 [21] A. J. Kaizer, Modeling of the nonlinear response of an electrodynamic loudspeaker by a volterra series expansion, *Journal of the Audio Engineering Society* 35 (6) (1987) 421–433.
- [22] S. Brown, Linear and nonlinear loudspeaker characterization, Ph.D. thesis, Citeseer (2006).
- 570 [23] K. Lashkari, A novel volterra-wiener model for equalization of loudspeaker distortions, in: *Acoustics, Speech and Signal Processing, 2006. ICASSP 2006 Proceedings. 2006 IEEE International Conference on*, Vol. 5, IEEE, 2006, pp. V–V.
- 575 [24] P. Brunet, B. Shafai, State-space modeling and identification of loudspeaker with nonlinear distortion, in: *Modelling, Identification, and Simulation, IASTED International Conference on*, Vol. 755, 2011.

- [25] M. Soria-Rodríguez, M. Gabouj, N. Zacharov, M. S. Hämäläinen, K. Koivuniemi, Modeling and real-time auralization of electrodynamic loudspeaker non-linearities, in: Acoustics, Speech, and Signal Processing, 2004. Proceedings.(ICASSP'04). IEEE International Conference on, Vol. 4, IEEE, 2004, pp. iv–81.
- [26] M. Dodd, Application of the finite element method to model the non-linear voice coil motion produced by a loudspeaker magnet assembly, PROCEEDINGS-INSTITUTE OF ACOUSTICS 23 (8) (2001) 1–14.
- [27] M. A. Dodd, et al., The application of fem to the analysis of loudspeaker motor thermal behaviour, in: Audio Engineering Society Convention 112, Audio Engineering Society, 2002.
- [28] M. H. Knudsen, J. G. Jensen, Low-frequency loudspeaker models that include suspension creep, Journal of the Audio Engineering Society 41 (1/2) (1993) 3–18.
- [29] B. R. Pedersen, F. T. Agerkvist, Time varying behavior of the loudspeaker suspension, in: Audio Engineering Society Convention 123, Audio Engineering Society, 2007.
- [30] M. Getzlaff, Fundamentals of magnetism, Springer Science & Business Media, 2007.
- [31] V. François-Lavet, F. Henrotte, L. Stainer, L. Noels, C. Geuzaine, Vectorial incremental nonconservative consistent hysteresis model, in: Proceedings of the 5th International Conference on Advanced Computational Methods in Engineering (ACOMEN2011), 2011.
- [32] A. Rumeau, Modélisation comportementale en génie électrique sous représentation diffusive: méthodes et applications, Ph.D. thesis, Université de Toulouse, Université Toulouse III-Paul Sabatier (2009).
- [33] C. Zuccatti, Thermal parameters and power ratings of loudspeakers, Journal of the Audio Engineering Society 38 (1/2) (1990) 34–39.
- [34] B. Maschke, A. J. Van Der Schaft, P. C. Breedveld, An intrinsic hamiltonian formulation of network dynamics: Non-standard poisson structures and gyrators, Journal of the Franklin institute 329 (5) (1992) 923–966.
- [35] A. Schaft, Port-hamiltonian systems: an introductory survey.
- [36] V. Duindam, A. Macchelli, S. Stramigioli, H. Bruyninckx, Modeling and Control of Complex Physical Systems: The Port-Hamiltonian Approach, Springer Science & Business Media, 2009.
- [37] A. Falaize, N. Lopes, T. Hélie, D. Matignon, B. Maschke, Energy-balanced models for acoustic and audio systems: a port-hamiltonian approach, Unfold Mechanics for Sounds and Music (2014) 1–8.

- [38] J.-J. E. Slotine, W. Li, et al., Applied nonlinear control, Vol. 199, Prentice-hall Englewood Cliffs, NJ, 1991.
- [39] J. E. Marsden, T. Ratiu, Introduction to mechanics and symmetry: a basic exposition of classical mechanical systems, Vol. 17, Springer Science & Business Media, 2013.
- [40] N. Lopes, T. Hélie, A. Falaize, Explicit second-order accurate method for the passive guaranteed simulation of port-hamiltonian systems, IFAC-PapersOnLine 48 (13) (2015) 223–228.
- [41] K. Thorborg, C. Futtrup, Frequency dependence of the loudspeaker suspension (a follow up), Journal of the Audio Engineering Society 61 (10) (2013) 778–786.
- [42] R. Koeller, Applications of fractional calculus to the theory of viscoelasticity, Journal of Applied Mechanics 51 (2) (1984) 299–307.
- [43] S. Holm, S. P. Nsholm, F. Prieur, R. Sinkus, Deriving fractional acoustic wave equations from mechanical and thermal constitutive equations, Computers & Mathematics with Applications 66 (5) (2013) 621 – 629, fractional Differentiation and its Applications.
- [44] S. Hu, W. Chen, X. Gou, Modal analysis of fractional derivative damping model of frequency-dependent viscoelastic soft matter, Advances in Vibration Engineering 10 (3) (2011) 187–196.
- [45] J. Sabatier, O. P. Agrawal, J. T. Machado, Advances in fractional calculus, Vol. 4, Springer, 2007.
- [46] R. Lewandowski, B. Chorażyczewski, Identification of the parameters of the kelvin–voigt and the maxwell fractional models, used to modeling of viscoelastic dampers, Computers & structures 88 (1) (2010) 1–17.
- [47] F. T. Agerkvist, T. Ritter, Modeling viscoelasticity of loudspeaker suspensions using retardation spectra, in: Audio Engineering Society Convention 129, Audio Engineering Society, 2010.
- [48] Y. Le Gorrec, D. Matignon, Diffusive systems coupled to an oscillator: a hamiltonian formulation, in: 4th IFAC Workshop on Lagrangian and Hamiltonian Methods for Non Linear Control, LHMNLC’12., 2012, pp. 1–6.
- [49] W. N. Findley, F. A. Davis, Creep and relaxation of nonlinear viscoelastic materials, Courier Corporation, 2013.
- [50] J. Vanderkooy, A model of loudspeaker driver impedance incorporating eddy currents in the pole structure, in: Audio Engineering Society Convention 84, Audio Engineering Society, 1988.

- [51] J. R. Wright, An empirical model for loudspeaker motor impedance, *Journal of the Audio Engineering Society* 38 (10) (1990) 749–754.
- [52] M. Dodd, W. Klippel, J. Ocleo-Brown, Voice coil impedance as a function of frequency and displacement, in: *Audio Engineering Society Convention 117*, Audio Engineering Society, 2004.
- [53] X.-P. Kong, F. Agerkvist, X.-W. Zeng, Modeling of lossy inductance in moving-coil loudspeakers, *Acta Acustica united with Acustica* 101 (3).
- [54] R. Buntenbach, A generalized circuit model for multiwinding inductive devices, *Magnetics, IEEE Transactions on* 6 (1) (1970) 65–65.
- [55] D. Hamill, Lumped equivalent circuits of magnetic components: the gyrator-capacitor approach, *Power Electronics, IEEE Transactions on* 8 (2) (1993) 97–103.
- [56] L. Laudebat, Modélisation et identification sous représentation diffusive de comportements dynamiques non rationnels en génie électrique, *These de l'Université Paul Sabatier, Toulouse*.
- [57] I. Schäfer, K. Krüger, Modelling of lossy coils using fractional derivatives, *Journal of Physics D: Applied Physics* 41 (4) (2008) 045001.
- [58] P. Brunet, B. Shafai, Identification of loudspeakers using fractional derivatives, *Journal of the Audio Engineering Society* 62 (7/8) (2014) 505–515.
- [59] H. Ramirez, B. Maschke, D. Sbarbaro, Modelling and control of multi-energy systems: an irreversible port-hamiltonian approach, *European Journal of Control* 19 (6) (2013) 513–520.
- [60] A. Chaigne, N. Quaegebeur, Influence of material and shape on sound reproduction by an electrodynamic loudspeaker, in: *Audio Engineering Society Convention 118*, Audio Engineering Society, 2005.
- [61] N. Quaegebeur, A. Chaigne, Nonlinear vibrations of loudspeaker-like structures, *Journal of Sound and Vibration* 309 (1-2) (2008) 178–196.
- [62] T. Hélie, D. Matignon, Representations with poles and cuts for the time-domain simulation of fractional systems and irrational transfer functions, *Signal Processing* 86 (10) (2006) 2516–2528.
- [63] T. Hélie, D. Matignon, Diffusive representations for the analysis and simulation of flared acoustic pipes with visco-thermal losses, *Mathematical Models and Methods in Applied Sciences* 16 (04) (2006) 503–536.

## AppendixA. Numerical method

685 To ensure stable simulation of stable dynamical system  $\frac{dx}{dt} = \mathbf{f}(x)$ , many numerical schemes focus on the approximation quality of the time derivative, combined with operation of the vector field  $\mathbf{f}$ . Here, we adopt an alternative point of view, by transposing the power balance (4) in the discrete time-domain to preserve passivity. This is achieved by numerical schemes that provide a 690 discrete version of the chain rule for computing the derivative of  $E = H \circ x$ . This is the case of Euler scheme, for which first order approximation of the differential applications  $dx(t, dt) = \frac{dx}{dt}(t) \cdot dt$  and  $dH(x, dx) = \nabla H(x)^T \cdot dx$  on the sample grid  $t \equiv kT, k \in \mathbb{Z}$  are given by

$$\delta x(k, T) = x(k+1) - x(k), \quad (\text{A.1})$$

$$\begin{aligned} \delta H(x, \delta x) &= H(x + \delta x) - H(x) \\ &= \nabla_d H(x, x + \delta x)^T \cdot \delta x. \end{aligned} \quad (\text{A.2})$$

For mono-variate storage components ( $H(x) = \sum_{n=1}^{n_x} H_n(x_n)$ ), the solution can be built element-wise with the  $n$ -th coordinate given by

$$[\nabla_d H(x, x + \delta x)]_n = \begin{cases} \frac{h_n(x_n + \delta x_n) - h_n(x_n)}{\delta x_n} & \text{if } \delta x_n \neq 0, \\ h'_n(x_n) & \text{otherwise.} \end{cases} \quad (\text{A.3})$$

A discrete chain rule is indeed recovered

$$\frac{\delta E(k, T)}{T} = \nabla^d H(x(k), x(k+1))^T \cdot \frac{\delta x(k, T)}{T} \quad (\text{A.4})$$

so that the following substitution in (3)

$$\begin{aligned} \frac{dx}{dt}(t) &\rightarrow \frac{\delta x(k, T)}{T} \\ \nabla H(x) &\rightarrow \nabla^d H(x(k), x(k+1)) \end{aligned} \quad (\text{A.5})$$

leads to

$$\begin{aligned} 0 &= \mathbf{a}(k)^T \cdot \mathbf{J} \cdot \mathbf{a}(k) = \mathbf{a}(k)^T \cdot \mathbf{b}(k) \\ &= \underbrace{\left[ \nabla^d H^T \cdot \frac{\delta x}{\delta t} \right] (k)}_{\frac{\delta E(k, T)}{T}} + \underbrace{\mathbf{z}(\mathbf{w}(k))^T \cdot \mathbf{w}(k)}_{P_D(k)} - \underbrace{\mathbf{u}(k)^T \cdot \mathbf{y}(k)}_{P_S(k)}. \end{aligned} \quad (\text{A.6})$$

For pH systems composed of a collection of linear energy storing components with quadratic Hamiltonian  $H_n(x_n) = \frac{x_n^2}{2C_n}$ , we define  $\mathbf{Q} = \text{diag}(C_1 \cdots C_{n_x})^{-1}$  so that the discrete gradient (A.3) reads

$$\nabla^d H(x, x + \delta x) = \mathbf{Q} \left( x(k) + \frac{\delta x(k)}{2} \right), \quad (\text{A.7})$$

which restores the midpoint rule. For nonlinear case, (A.3) leads to another 695 numerical scheme depending on the nonlinearity, still preserving passivity.

## AppendixB. Recalls on magnetism

### AppendixB.1. Magnetic energy storage

*Definitions.* The magnetic phenomena are described by two complementary fields, namely, the applied magnetic excitation  $\mathbf{h}$  and the induced magnetic flux density  $\mathbf{b}(\mathbf{h})$ , which is somewhat the response of a given material to a given excitation. The induction  $\mathbf{b}$  is defined as the superposition of the magnetization of vacuum  $\mathbf{j}_0(\mathbf{h})$  and the magnetization of matter  $\mathbf{j}(\mathbf{h})$  due to microscopic magnetic moments attached to the atoms of the body (see [30, (1.6)] and [31, (6)]):

$$\mathbf{b} = \mathbf{j}_0(\mathbf{h}) + \mathbf{j}(\mathbf{h}) \simeq \mathbf{j}(\mathbf{h})$$

where we neglect the magnetization of vacuum so that  $\mathbf{h}(\mathbf{b}) = \mathbf{j}^{-1}(\mathbf{b})$ . The magnetic induction flux  $\phi$  is defined as the flux of the magnetic induction field through a given surface  $\mathcal{S}$ :  $\phi(t) = \iint_{\mathcal{S}} b(t) dS = S b(t)$ , where we assumed constant  $\mathbf{b} \equiv b(t)$  over  $\mathcal{S}$ . The *magnetomotive force*  $\psi$  is defined as the circulation of  $\mathbf{h}$  along a closed  $\mathbf{b}$ -field line  $\mathcal{C}$  with length  $\ell_C$ :  $\psi(b(t)) = \oint_{\mathcal{C}} h(b(t)) dl = \ell_C \cdot h(b(t))$ , where we assumed constant  $\mathbf{h} \equiv h(b(t))$  along  $\mathcal{C}$ .

*Energy storage.* The variation of magnetic energy density stored in a sample of magnetic material is  $\frac{dE}{dt} = h(b) \frac{db}{dt}$  (see e.g. [31] for details). The total energy variation for a sample with length  $\ell_C$  and section  $S$  ( $\text{m}^2$ ) is then  $\frac{dE}{dt} = S \ell_C h(b) \frac{db}{dt} = \psi \left( \frac{\phi}{S} \right) \frac{d\phi}{dt}$ . The associated storage function (Hamiltonian) is defined by

$$H_{\text{mag}}(\phi) = \ell_C \int_0^\phi h \left( \frac{x}{S} \right) dx \quad (\text{B.1})$$

which restores the total energy variation  $\frac{d}{dt} H_{\text{mag}} = \psi \frac{d\phi}{dt}$ .

### AppendixB.2. Electromechanical coupling

Consider several windings of a conductive wire with section  $S_w$ , length  $\ell_w$ , position  $q_w$  and velocity vector  $\mathbf{v}_w = v_w \mathbf{e}_w$  with constant direction  $\mathbf{e}_w$  and magnitude  $v_w = \frac{dq_w}{dt}$ . This conductor is immersed in a magnetic induction field  $\mathbf{b}$  with constant direction orthogonal to  $\mathbf{e}_w$  and constant magnitude  $B$ . The current is  $i_w = \iint_{S_w} \rho_q \mathbf{v}_q dS$  for the electric charge density  $\rho_q$  moving with velocity  $\mathbf{v}_q = v_q \mathbf{e}_q$  and unitary vector  $\mathbf{e}_q$  normal to the surface  $S_w$ . A wire element with length  $dl$  is subjected to the Lorentz force  $d\mathbf{f}_{\mathcal{L}} = \rho_q S_w dl (\mathbf{v}_q + \mathbf{v}_w) \times \mathbf{b}$ . This force is orthogonal to the velocity  $\mathbf{v}_q + \mathbf{v}_w$  so that the associated mechanical power is  $dP_{\mathcal{L}} = d\mathbf{f}_{\mathcal{L}} \cdot (\mathbf{v}_q + \mathbf{v}_w) = 0$ . Integrating along the wire, one gets

$$P_{\mathcal{L}} = v_w \cdot \underbrace{B \ell_w i_w}_{f_{\mathcal{L}}} + i_w \underbrace{B \ell_w v_w}_{v_{\mathcal{L}}} = 0 \quad (\text{B.2})$$

defining the Lorentz force  $f_{\mathcal{L}}$  and the back electromotive force (voltage)  $v_{\mathcal{L}}$ . Notice the transfer is reversible and conservative in the sense that the outflow

of energy from the electrical domain  $P_{\text{elec}} = v_w f_{\mathcal{L}}$  equals the inflow of the mechanical domain  $P_{\text{meca}} = v_w f_{\mathcal{L}}$ , that is  $P_{\mathcal{L}} = P_{\text{meca}} - P_{\text{elec}} = 0$ . This corresponds to a gyrator with ratio  $B \ell_w$ :

$$\begin{pmatrix} v_{\mathcal{L}} \\ f_{\mathcal{L}} \end{pmatrix} = \begin{pmatrix} 0 & -B \ell_w \\ B \ell_w & 0 \end{pmatrix} \cdot \begin{pmatrix} i_w \\ v_w \end{pmatrix}. \quad (\text{B.3})$$

### Appendix B.3. electromagnetic coupling: the gyrator-capacitor approach

The gyrator-capacitor approach introduced in the late sixties [54, 55] is an easy way to develop electronic analog of magnetic circuits. It has been considered in [14] for the modeling of the loudspeaker. In this approach, a coil is divided in a gyrator (wire turns) and a magnetic energy storage (coil core).

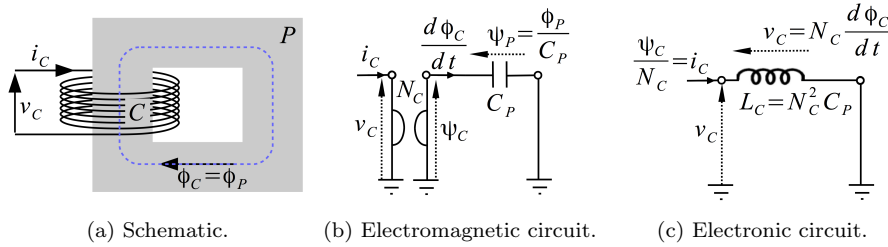


Figure B.20: Simple electromagnetic circuit that includes a coil ( $C$ ) with  $N_c$  wire turns and a magnetic path ( $P$ ) with associated magnetic capacity  $C_p$ . According to the *gyrator-capacitor* approach, the coil is modeled as an electromagnetic gyrator with  $\psi_c = N_c i_c$  and  $v_c = N_c \frac{d\phi_c}{dt}$ .

710

The dynamics of a magnetic field can be described by two complementary macroscopic quantities: the *magnetic induction field*  $\psi$  and the *magnetomotive force* (mmf)  $\psi$  (see Appendix B.1). The electromagnetic transfer for a single wire turn stands from (i) *Faraday's law* of electromagnetic induction that relates the electromotive force (tension  $v$ ) to the variation of the magnetic flux in the wire turn  $v = \frac{d\phi}{dt}$ ; and (ii) *Ampère's theorem* that relates the mmf to the current in the wire  $\psi = i$  [54, 55]. Considering the coil ( $C$ ) in figure B.20a with  $N_c$  wire turns around the path ( $P$ ), these relations restores a gyrator with ratio  $N_c$ :

$$\begin{pmatrix} v_c \\ \psi_c \end{pmatrix} = \begin{pmatrix} 0 & N_c \\ N_c & 0 \end{pmatrix} \begin{pmatrix} i_c \\ \frac{d\phi_c}{dt} \end{pmatrix}. \quad (\text{B.4})$$

Denoting by  $s \in \mathbb{C}$  the Laplace variable, the correspondence between an impedance seen in the electrical domain  $Z_{\text{elec}}(s) = \frac{v_c(s)}{i_c(s)}$  and its counterpart in the magnetic domain  $Z_{\text{mag}}(s) = \frac{\psi_c(s)}{s \phi_c(s)} = \frac{N_c^2 i_c(s)}{v_c(s)}$  is given by

$$Z_{\text{mag}}(s) = \frac{N_c^2}{Z_{\text{elec}}(s)}, \quad (\text{B.5})$$

so that the electrical inductance associated with the magnetic capacity is  $L_c = N_c^2 C_p$ . Notice the interconnection (B.4) is conservative:  $P_{\text{elec}} = P_{\text{mag}}$  with  $P_{\text{elec}} = v_c i_c$

the power outgoing the electrical domain and  $P_{\text{mag}} = \frac{d\phi_c}{dt} \psi_c$  the power incoming the magnetic domain.

### 715 AppendixC. State saturating storage function

The saturation effect of the suspension (phenomenon 5) and the ferromagnetic path (phenomenon 6) are described by the same idealized (symmetric) saturation curve  $c(x)$  shown in figure-C.21a. It is built as the linear combination of basis functions  $c_{\text{lin}}(x)$  (linear behavior around the origin) and  $c_{\text{sat}}(x)$  (saturation effect):  
720

$$c(x) = P_{\text{lin}}(c_{\text{lin}}(x) + P_{\text{sat}}c_{\text{sat}}(x)), \quad (\text{C.1})$$

$$c_{\text{lin}}(x) = x, \quad (\text{C.2})$$

$$c_{\text{sat}}(x) = \frac{4}{4 - \pi} \left( \tan \left( \frac{\pi \cdot x}{2x_{\text{sat}}} \right) - \frac{\pi \cdot x}{2x_{\text{sat}}} \right) \quad (\text{C.3})$$

with  $c_{\text{sat}}(x) \xrightarrow{x \rightarrow \pm x_{\text{sat}}} \pm \infty$ ,  $\frac{\partial c_{\text{sat}}}{\partial x}(0) = 0$  so that  $c_{\text{sat}}(x)$  does not contribute around origin, and  $c_{\text{sat}}(\frac{1}{2}) = 1$ .

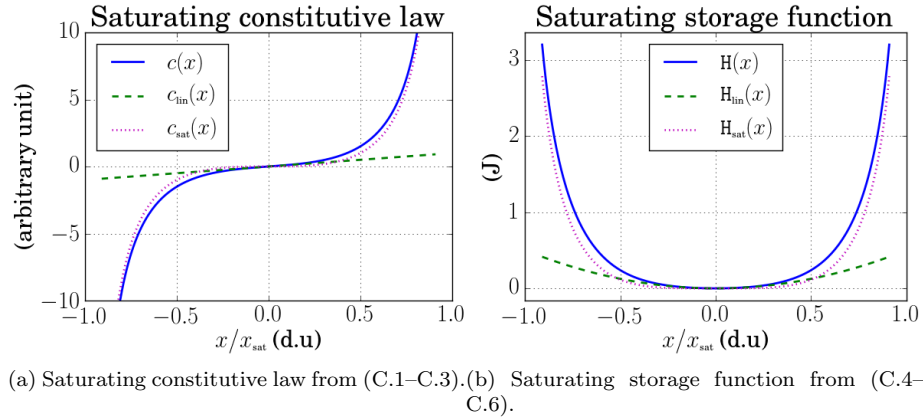


Figure C.21: Generic state saturating constitutive law and associated storage function to be used for the modeling of stress-strain relation of the suspension material (S) and magnetic excitation-induction relation for path material (P). Parameters are  $P_{\text{lin}} = P_{\text{sat}} = x_{\text{sat}} = 1$ .

The corresponding Hamiltonian (see figure C.21b) is obtained from

$$H(x) = \int_0^x c(\xi) d\xi = P_{\text{lin}}(H_{\text{lin}}(x) + P_{\text{sat}}H_{\text{sat}}(x)) \quad (\text{C.4})$$

with

$$H_{\text{lin}}(x) = \frac{x^2}{2}, \quad (\text{C.5})$$

$$H_{\text{sat}}(x) = -\frac{8x_{\text{sat}}}{\pi(4 - \pi)} \left( \ln \left| \cos \left( \frac{\pi x}{2x_{\text{sat}}} \right) \right| + \frac{1}{2} \left( \frac{\pi x}{2x_{\text{sat}}} \right)^2 \right). \quad (\text{C.6})$$

This nonlinear saturating storage function proves positive definite providing the parameters  $(P_{\text{lin}}, P_{\text{sat}})$  are positive, so that it can be used in structure (3), still preserving passivity.

## AppendixD. Fractional order dynamics

The diffusive process in the suspension (creep phenomenon 4) and the ferromagnetic path (eddy current phenomenon 7) can be described by linear models that include fractional order dynamics (see [42, 46, 44, 43] for fractional modeling of viscoelasticity, and [57, 56, 32] for fractional modeling of eddy currents). A well established formalism for the realization of fractional transfer functions is the so called *diffusive representations*, recalled thereafter (see detailed developments in [62, 63], and [48] for a port-Hamiltonian formulation).

### AppendixD.1. Fractional integrator

Defining  $s = \rho e^{i\theta}$ , with  $\rho \geq 0$  and  $\theta \in [-\pi, \pi[$ , the transfer function of the fractional integrator  $\mathcal{I}_\beta(s) = s^{-\beta}$  exhibits a cut  $\mathcal{C} = \mathbb{R}_-$ . The residue theorem gives the realization of  $\mathcal{I}_\beta$  as the continuous aggregation of linear damping along the cut  $\mathcal{C}$ . This leads to the following *diffusive representation* [48, §2]:

$$\begin{aligned} \mathcal{I}_\beta(s) : \mathbb{C} \setminus \mathbb{R}_- &\rightarrow \mathbb{C} \\ s &\mapsto \int_0^\infty \mu_\beta(\xi) \frac{1}{s+\xi} d\xi \end{aligned} \quad (\text{D.1})$$

where the weights  $\mu_\beta(\xi) = \frac{\mathcal{I}_\beta(-\xi-i0^+) - \mathcal{I}_\beta(-\xi+i0^+)}{2i\pi} = \frac{\sin(\beta\pi)}{\pi} \xi^{-\beta}$  correspond to the jump of  $\mathcal{I}_\beta$  across  $\mathcal{C} \equiv \{-\xi \in \mathbb{R}^-\}$ . A state-space representation with output  $y_\beta(s) = \mathcal{I}_\beta(s)u_\beta(s)$  is:

$$\begin{cases} \frac{dx_\xi}{dt} = -\xi x_\xi + u_\beta, & x_\xi(0) = 0, \\ y_\beta = \int_0^{+\infty} \mu_\beta(\xi) x_\xi d\xi. \end{cases} \quad (\text{D.2})$$

The system (D.2) is recast as an infinite dimensional pH system (3), defining the *hamiltonian density*  $H_\xi(x_\xi) = \mu_\beta(\xi) \frac{x_\xi^2}{2}$  and the *resistance density*  $r_\xi = \frac{\xi}{\mu_\beta(\xi)}$  with  $z_\xi(w_\xi) = r_\xi w_\xi$ :

$$\begin{pmatrix} \frac{dx_\xi}{dt} \\ w_\xi \\ y_\beta \end{pmatrix} = \begin{pmatrix} 0 & -1 & 1 \\ 1 & 0 & 0 \\ \mathbb{1}_\infty & 0 & 0 \end{pmatrix} \begin{pmatrix} \frac{\partial H_\xi}{\partial x_\xi} \\ z_\xi(w_\xi) \\ u_\beta \end{pmatrix} \quad (\text{D.3})$$

where  $\mathbb{1}_\infty$  denotes an infinite dimensional row vector of 1, that is  $y_\beta = \int_0^\infty \frac{\partial H_\xi}{\partial x_\xi} d\xi$ . Notice the total energy is  $H_\beta(\mathbf{x}_\beta) = \int_{\xi \in \mathcal{C}} H_\xi(x_\xi) d\xi$  with infinite dimensional state  $\mathbf{x}_\beta \in \mathbb{R}^{\mathbb{R}^+}$ . The realization of the dynamical element with parameter  $p$  and transfer function  $\mathcal{I}_{p,\beta}(s) = (ps^\beta)^{-1}$  is given by (D.3), with  $\tilde{\mu}_{\beta,p}(\xi) = \frac{\mu_\beta(\xi)}{p}$ .

Fractional damping can be modeled as combination of fractional integrators and differentiators (see [42, 63, 45, 48]). The realization of fractional differentiator of order  $\alpha$  with input  $u_\alpha$ , transfer function  $\mathcal{D}_\alpha(s) = s^\alpha$  and output  $y_\alpha = \mathcal{D}_\alpha u_\alpha$ , is built on the diffusive representation (D.2) as follows [63, 48]:

$$\begin{cases} \frac{dx_\xi}{dt} = -\xi \cdot x_\xi + u_\alpha, & x_\xi(0) = 0, \\ y_\alpha = \int_0^{+\infty} \mu_{1-\alpha}(\xi)(u_\alpha - \xi \cdot x_\xi) d\xi. \end{cases} \quad (\text{D.4})$$

Defining the *hamiltonian density*  $H_\xi(x_\xi) = \mu_{1-\alpha}(\xi)\xi \frac{x_\xi^2}{2}$ , the *resistance density*  $r_\xi = \mu_{1-\alpha}(\xi)$  and  $z_\xi(w_\xi) = r_\xi w_\xi$ , the pH formulation of the fractional differentiator (D.4) is

$$\begin{pmatrix} \frac{dx_\xi}{dt} \\ w_\xi \\ y_\alpha \end{pmatrix} = \begin{pmatrix} 0 & -\frac{1}{\mu_{1-\alpha}(\xi)} & 0 \\ \frac{1}{\mu_{1-\alpha}(\xi)} & 0 & -1 \\ 0 & -1_\infty & 0 \end{pmatrix} \begin{pmatrix} \frac{\partial H_\xi}{\partial x_\xi} \\ z_\xi(w_\xi) \\ u_\alpha \end{pmatrix}. \quad (\text{D.5})$$

### *Appendix D.3. Finite order approximation*

For implementation purpose, a finite approximation of diffusive representation (D.3) is built based on a finite set of  $n_\xi$  poles  $(\xi_1, \dots, \xi_{n_\xi})$  localized on the cut  $\mathcal{C}$ . The weights  $\boldsymbol{\mu} = (\mu_1 \cdots \mu_{n_\xi})^T$  are obtained from a least square optimization as detailed in [63, sec. 5.1.2], by minimizing an appropriate distance between  $\mathcal{I}_\beta$  and its discretisation  $\widehat{\mathcal{I}}_\beta$ :

$$\widehat{\mathcal{I}}_\beta(s) = \sum_{n=1}^{n_\xi} \frac{\mu_n}{s + \xi_n} = \mathbf{E}(s) \cdot \boldsymbol{\mu} \quad \text{with} \quad \mathbf{E}(s) = \left( \frac{1}{s + \xi_1} \cdots \frac{1}{s + \xi_{n_\xi}} \right)^T. \quad (\text{D.6})$$

The poles  $\xi_n$ 's are chosen as  $\xi_n = 10^{\ell_n} \in \mathcal{C}$ , for  $0 \leq n \leq n_\xi + 1$ , where the  $\ell_n$ 's are equally spaced, with step  $\delta = \frac{\ell_{n_\xi+1} - \ell_0}{n_\xi+1}$ , from  $\ell_0$  to  $\ell_{N+1}$ . Since gain deviations are perceived relatively to the reference gains on the audio range, the weights  $\boldsymbol{\mu}$  are optimized with respect to the objective function

$$\mathcal{O}(\boldsymbol{\mu}) = \int_{\omega_-}^{\omega_+} \left| 1 - \frac{\widehat{\mathcal{I}}_\beta(s=i\omega)}{\mathcal{I}_\beta(s=i\omega)} \right|^2 d \ln \omega. \quad (\text{D.7})$$

where  $\omega_- = 2\pi f_-$ ,  $\omega_+ = 2\pi f_+$  for  $[f_-, f_+] = [20\text{Hz}, 20\text{kHz}]$ . In practice, the integral in (D.7) is approximated by a finite sum on a frequency grid, here,  $\ln \omega_k = \ln \omega_- + \frac{k}{n_\omega} \ln \frac{\omega_+}{\omega_-}$  for  $0 \leq k \leq n_\omega$ . This yields the following practical objective function

$$\widehat{\mathcal{O}}(\boldsymbol{\mu}) = \overline{(\mathbf{M}\boldsymbol{\mu} - \mathbf{T})^T \mathbf{W}(\mathbf{M}\boldsymbol{\mu} - \mathbf{T})}, \quad (\text{D.8})$$

where matrix  $\mathbf{M}$  is composed of the rows  $[\mathbf{M}]_{k,:} = \mathbf{E}(s = i\omega_{k-\frac{1}{2}})^T$  defined in (D.6), where  $\omega_{k-\frac{1}{2}} = \sqrt{\omega_{k-1}\omega_k}$  denotes the mean of  $\omega_{k-1}$  and  $\omega_k$  for  $1 \leq$

$k \leq n_\omega$ . Vector  $\mathcal{I}$  is composed of  $[\mathcal{I}]_k = \mathcal{I}_\beta(s = i\omega_{k-\frac{1}{2}})$  and the diagonal matrix  $\mathbf{W}$  is defined by  $[\mathbf{W}]_{k,k} = (\ln \omega_k - \ln \omega_{k-1}) / |[\mathcal{I}]_k|^2$ . The minimization of (D.8) is achieved by off-the-shelf optimization algorithm, imposing the weights to be positive:

$$\hat{\boldsymbol{\mu}} = \{\min_{\boldsymbol{\mu}} \hat{\mathcal{O}}(\boldsymbol{\mu}) : \boldsymbol{\mu} > 0\} \quad (\text{D.9})$$

The finite dimensional pH system realizing the weighted fractional integrator with transfer function  $\mathcal{I}_{p,\beta} = (ps^\beta)^{-1}$  is given in table D.9 with:

$$\begin{cases} p_n &= \frac{\hat{\boldsymbol{\mu}}_n}{\xi_n^p}, \\ r_n &= \frac{p}{p_n}, \end{cases} \quad n \in (1, \dots, n_\xi). \quad (\text{D.10})$$

According to section AppendixD.2, the finite dimensional approximation of the

State: $\mathbf{x}_\beta = (x_1, \dots, x_{n_\xi})^\top$	Energy: $H_\beta(\mathbf{x}_\beta) = \frac{1}{2} \mathbf{x}_\beta^\top \text{diag}(p_1, \dots, p_{n_\xi}) \mathbf{x}_\beta$
Dissipation variable: $\mathbf{w}_\beta = (w_1, \dots, w_{n_\xi})^\top$	Dissipation law: $\mathbf{z}_\beta(\mathbf{w}_\beta) = \text{diag}(r_1, \dots, r_{n_\xi}) \mathbf{w}_\beta$
Input: $u_\beta$	Output: $\hat{y}_\beta$
Structure: $\mathbf{J}_x = \mathbb{0}_{n_\xi \times n_\xi}, \mathbf{K} = \mathbb{I}_{n_\xi}, \mathbf{G}_x = \mathbb{1}_{n_\xi \times 1},$ $\mathbf{J}_w = \mathbb{0}_{n_\xi \times n_\xi}, \mathbf{G}_w = \mathbb{0}_{n_\xi \times 1}, \mathbf{J}_y = 0.$	

Table D.9: Port-Hamiltonian formulation (3) for the approximation of the fractional integrator  $y_\beta(s) = (ps^\beta)^{-1} u_\beta(s)$  on a finite set of  $n_\xi$  poles. The parameters  $p_n, r_n$  for  $n \in (1, \dots, n_\xi)$  are defined in (D.10) based on the minimization of (D.8). As an example, if  $u_\beta \equiv i$  and  $y_\beta \equiv v$ , this structure corresponds to the serial connection of  $n_\xi$  parallel RC cells; if  $y_\beta \equiv i$  and  $u_\beta \equiv v$ , this structure corresponds to the parallel connection of  $n_\xi$  serial LC cells.

weighted fractional differentiator with transfer function  $\mathcal{D}_{\alpha,p} = ps^\alpha$  is obtained from the minimization of (D.8) for the transfer function  $\mathcal{I}_{1-\alpha}$ . The corresponding pH formulation is given in table D.10 with:

$$\begin{cases} p_n &= p \hat{\boldsymbol{\mu}}_n \xi_n, \\ r_n &= p_n \hat{\boldsymbol{\mu}}_n, \end{cases} \quad n \in (1, \dots, n_\xi). \quad (\text{D.11})$$

State: $\mathbf{x}_\alpha = (x_1, \dots, x_{n_\xi})^\top$	Energy: $H_\alpha(\mathbf{x}_\alpha) = \frac{1}{2} \mathbf{x}_\alpha^\top \text{diag}(p_1, \dots, p_{n_\xi}) \mathbf{x}_\alpha$
Dissipation variable: $\mathbf{w}_\alpha = (w_1, \dots, w_{n_\xi})^\top$	Dissipation law: $\mathbf{z}_\alpha(\mathbf{w}_\alpha) = \text{diag}(r_1, \dots, r_{n_\xi}) \mathbf{w}_\alpha$
Input: $u_\alpha$	Output: $\tilde{y}_\alpha$
Structure: $\mathbf{J}_x = \mathbb{0}_{n_\xi \times n_\xi}, \mathbf{K} = \text{diag}(\hat{\mu})^{-1}, \mathbf{G}_x = \mathbb{0}_{n_\xi \times 1},$ $\mathbf{J}_w = \mathbb{0}_{n_\xi \times n_\xi}, \mathbf{G}_w = -\mathbb{1}_{n_\xi \times 1}, \mathbf{J}_y = 0.$	

Table D.10: Port-Hamiltonian formulation (3) for the approximation of the fractional differentiator  $y_\alpha(s) = ps^\alpha u_\alpha(s)$  on a finite set of  $n_\xi$  poles. The parameters  $p_n, r_n$  for  $n \in (1, \dots, n_\xi)$  are defined in (D.11) based on the minimization of (D.8) for the transfer function  $\mathcal{I}_{1-\alpha}$ . The interpretation is less intuitive than for the fractional integrator of table D.9 due to the coefficients in  $\mathbf{K}$  that involves transformers.

## AppendixE. Physical and technological parameters

In the sequel, acronym *d.u.* stands for *dimensionless unit*.

<sup>745</sup> AppendixE.1. Model 0

Label	Description	Typical value	Unit
$R_c$	Electrical DC Resistance of coil wire	10	$\Omega$
$L_c$	Coil self inductance	$3.10^{-4}$	H
$M_{CDA}$	Total mass of the moving part	$10^{-2}$	Kg
$K_{SA}$	Total stiffness	$2.10^3$	$N.m^{-1}$
$R_{SA}$	Mechanical resistance	1	$N.s.m^{-1}$
$B_\ell$	Force factor	5	T.m
$\ell_c^0$	Total length of coil wire	10	m
$B$	Magnetic induction magnitude	$B_\ell/\ell_c^0$	T
$Q_\ell$	Overhang parameter in (8)	$5.10^{-3}$	m
$P_\ell$	Shape parameter in (8)	5	<i>d.u.</i>

Table E.11: Physical and technological parameters involved in the model 0 of table 3. Typical values are chosen in accordance with data provided in [2, table 3.1] for the DALI 311541 6 1/2" unit.

AppendixE.2. Model 1

Label	Description	Typical value	Unit
$\tau_{ve}$	Characteristic creep time	1	s
$\alpha_{ve}$	Memory parameter	0.5	d.u.
$P_K$	Distribution of $K_{SA}$ between $K_0$ and $K_1$	0.6	d.u.
$n_{ve}$	Number of poles for approximation (15)	20	d.u.
$\xi_n$	Finite set of poles for approximation (15)	$[10^{-5}, \dots, 10^5]$	Hz
$K_0$	Primary stiffness	$\frac{K_{SA}}{P_K}$	$N.m^{-1}$
$q_{sat}$	Saturation position associated with primary elongation	$10^{-2}$	m
$P_{sat}^S$	Shape parameter for nonlinear stress-strain relation	10	d.u.
$\omega_1$	Characteristic creep frequency	$\frac{2\pi}{\tau_{ve}}$	Hz
$K_1$	Characteristic creep stiffness	$\frac{K_{SA}}{2(1-P_K)}$	$N.m^{-1}$
$R_1$	Characteristic creep damping	$\frac{K_1}{\omega_1}$	$N.s.m^{-1}$

Table E.12: Physical and technological parameters involved in creep model in table 4 and model 1 in table 5. Typical values are chosen in accordance with [17, table 1].

#### AppendixE.3. Model 2

Label	Description	Typical value	Unit
$N_c$	Number of coil wire turns	100	d.u.
$A_c$	Height of the coil wire turns	$10^{-2}$	m
$D_c$	Coil diameter	$2.10^{-2}$	m
$\psi_M$	Magnetomotive force imposed by the magnet (M)	see (24)	A
$S_g$	Area of the magnetic flux in the air gap (G)	$\pi D_c A_c$	$m^2$
$S_p$	Area of the magnetic flux in the pole piece (P)	$S_g$	$m^2$
$\phi_{ss}$	Steady-state magnetic flux in the path (P, G)	$\frac{B}{S_p}$	Wb
$\ell_p$	Mean length of flux loops in the path (P, G)	$10^{-1}$	m
$L_{leak}$	Inductance associated with the leakage flux	$10^{-6}$	H
$C_{ss}$	Steady-state magnetic capacity of path PG	see (29)	H
$\tau_{PG}$	Characteristic time associated with the flux $\phi_{PG}$	10	s
$\omega_{PG}$	Characteristic frequency associated with the flux $\phi_{PG}$	$\frac{2\pi}{\tau_{PG}}$	Hz
$\omega_{ec}$	Characteristic frequency associated with eddy currents	see (30)	Hz
$\alpha_{ec}$	Eddy currents memory parameter	0.5	d.u.
$C_{ec}$	Eddy currents characteristic magnetic capacity	see (29)	H
$R_{ec}$	Eddy currents characteristic magnetic resistance	$\frac{C_{ec}}{\omega_{ec}}$	$\Omega^{-1}$

Table E.13: Physical and technological parameters involved in the model 2 in figures 11 and 14. Typical values are chosen in accordance with [16, table 3].

#### AppendixE.4. Model 3

Label	Description	Typical value	Unit
$C_c$	Heat capacity of coil wire	2.358	$\text{J.K}^{-1}$
$C_g$	Heat capacity of air gap	71.49	$\text{J.K}^{-1}$
$C_p$	Heat capacity of pole piece	664.3	$\text{J.K}^{-1}$
$C_a$	Heat capacity of air in enclosure	$10^4$	$\text{J.K}^{-1}$
$R_{cg}$	Thermal resistance between coil wire and air gap	3.927	$\text{K.W}^{-1}$
$R_{gp}$	Thermal resistance between air gap and pole piece	1.158	$\text{K.W}^{-1}$
$R_{pa}$	Thermal resistance between pole piece and environment	2.623	$\text{K.W}^{-1}$
$\alpha_\tau$	Temperature coefficient of copper	$4.10^{-3}$	$\text{K}^{-1}$

Table E.14: Physical and technological parameters involved in the model 3 of figure 17. Typical values for thermal capacity and resistance are taken from [13, § 4.4.3]. The temperature coefficient of copper is taken from [13, eq. (14)].

## Appendix F. Additional simulation results

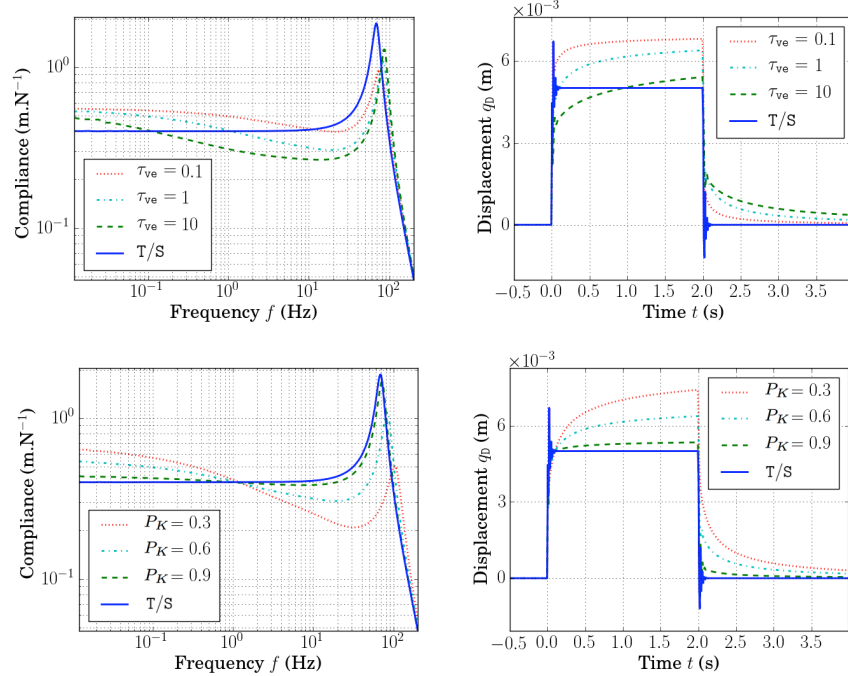
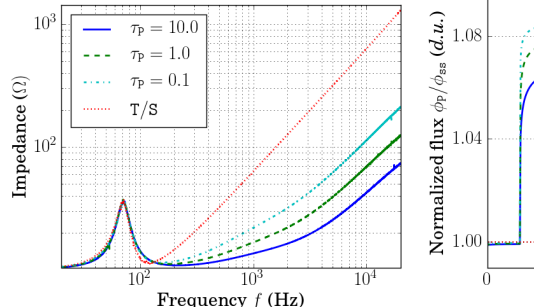
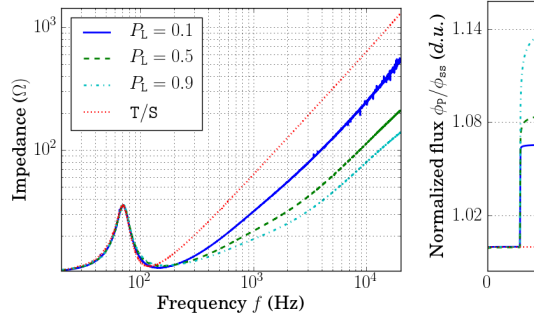


Figure F.22: Simulation of the small-signal modeling of the mechanical subsystem in table 4 depicted in figure 7 with the parameters in tables E.11 and E.12 (except creep time  $\tau_{ve}$  and partition parameter  $P_K$  indicated in the legend). Sample rate is 96kHz. Left: diaphragm displacement in response to the Lorentz force  $\left| \frac{q_D}{f_C} \right| (2i\pi f)$  (frequency domain on the range [0.01,200]Hz). Right: diaphragm displacement in response to a 10N Lorentz force step between 0s and 2s (time domain). Legend T/S refers to the mechanical subsystem of the Thiele/Small modeling. Results for the memory parameter  $\alpha_{ve}$  are given in figure 9.

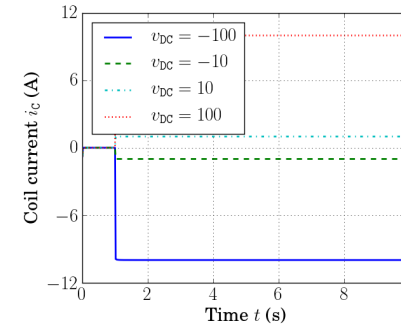


(a) Influence of characteristic time  $\tau_{PG} = \frac{2\pi}{\omega_{PG}}$ .

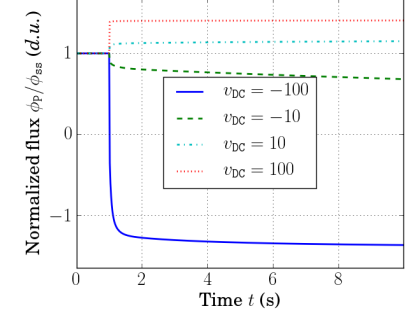


(b) Influence of partition parameter  $p_L$ .

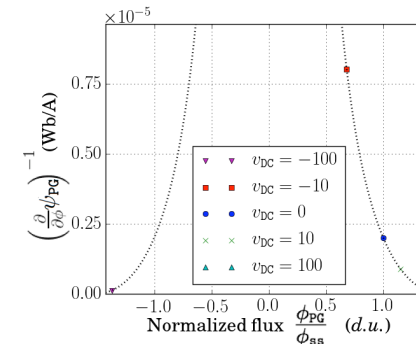
Figure F.23: Simulation of the loudspeaker model 2 in table 6 depicted in figure 14 with the parameters in tables E.11 and E.13 (except memory parameter indicated in the legend). Sample rate is 96kHz. Left: normalized flux  $\frac{\phi_{PG}}{\phi_{ss}}$  in response to a 10V step voltage between 1s and 4s. Right: modulus of electrical impedance  $\left| \frac{v_1(2i\pi f)}{i_c(2i\pi f)} \right|$ . Legend T/S refers to the Thiele/Small modeling. Results for the memory parameters  $\alpha_{ec}$  are given in figure 15.



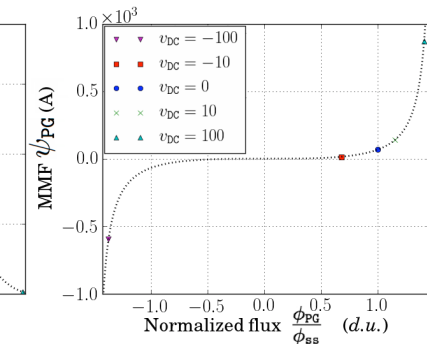
(a) Evolution of current



(b) Evolution of flux  $\phi_{PG}/\phi_{ss}$



(c)  $C_{ss}$  from (25).



(d) magnetomotive force  $\psi_{PG}(\phi_{PG})$  from (22).

Figure F.24: Results associated with figure 16 for the model 2. The input voltage is  $v_I(t) = v_{DC}$ , thus changing the steady-state magnetic flux  $\phi_{ss}$ , hence the equivalent magnetic capacity  $C_{ss} = \left( \frac{\partial^2 H_p}{\partial \phi_p^2}(\phi_{ss}) \right)^{-1}$  according to (25).